

₁ Physics-Infused Reduced-Order Modeling for Analysis of
₂ Ablating Hypersonic Thermal Protection Systems

₃

₄ November 26, 2025

₅

Abstract

₆ This work presents a *physics-infused reduced-order modeling* (PIROM) framework
₇ towards design, analysis, and optimization of non-decomposing ablating hypersonic
₈ thermal protection systems (TPS), and is demonstrated via the modeling of transient
₉ thermo-ablative responses of multi-layered hypersonic TPS. The PIROM architecture
₁₀ integrates a *reduced-physics model* (RPM) as the building block, which is based on
₁₁ the *lumped capacitance model* (LCM) coupled to a *surface recession model* (SRM).
₁₂ The RPM provides a low-fidelity estimate of the thermo-ablative response of the TPS,
₁₃ based on average temperatures and one-dimensional surface displacements. This RPM
₁₄ is extended with data-driven hidden dynamics that are formulated via a systematic
₁₅ coarse-graining approach rooted in the *Mori-Zwanzig* (MZ) formalism, and that are
₁₆ learned from high-fidelity simulation data. Therefore, while the LCM and SRM capture
₁₇ the dominant physics of the ablating TPS response, the correction terms compensate for
₁₈ residual dynamics arising from higher-order non-linear interactions and temperature-
₁₉ advection effects due to surface recession. The trained PIROM consistently achieves
₂₀ errors of $\approx 0.5\%$ for a wide range of extrapolative settings of design parameters involv-
₂₁ ing time-and-space varying boundary conditions and SRM models, and improves by an
₂₂ order of magnitude by the LCM alone. Moreover, the PIROM delivers RPM-level com-
₂₃ putational costs, enabling evaluations that are two orders of magnitude faster than
₂₄ the high-fidelity full-order model (FOM). These results demonstrate that PIROM ef-
₂₅ fectively reconciles the trade-offs between accuracy, generalizability, and efficiency, pro-
₂₆ viding a promising framework for optimizing multi-physical dynamical systems, such
₂₇ as TPS, under diverse operating conditions.

₂₈

1 Introduction

₂₉ At hypersonic speeds, aerospace vehicles experience extreme aero-thermo-dynamic environ-
₃₀ ments that require specialized thermal protection systems (TPS) to shield internal sub-
₃₁ structures, electronics, and possibly crew members from the intense aerodynamic heating.
₃₂ The TPS is composed of ablating materials to withstand the high-energy physics – a high-
₃₃ temperature-capable and fibrous material injected with a resin that fills the pore network
₃₄ and strengthens the composite [1]. The TPS design promotes the exchange of mass through
₃₅ thermal and chemical reactions (i.e., ablation), effectively mitigating heat transfer to the

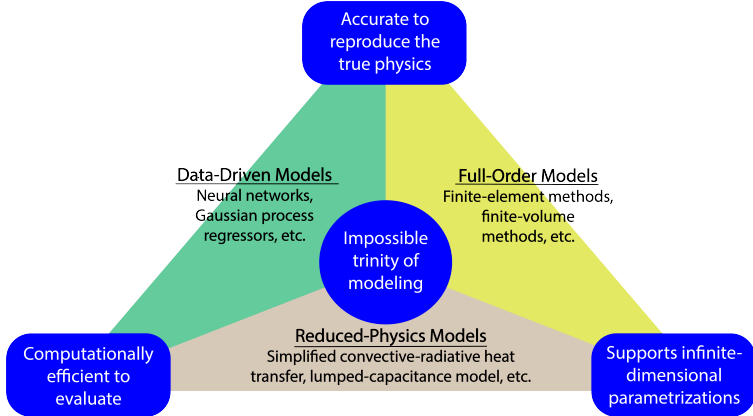


Figure 1: The impossible trinity of modeling: accuracy, generalizability, and efficiency.

36 sub-structures. As a result, accurate prediction for the ablating TPS response under ex-
 37 treme hypersonic heating becomes critical to ensuring survivability, performance, and safety
 38 of hypersonic vehicles.

39 Even with today’s advancements in computational resources and numerical methods,
 40 high-fidelity simulations of ablating TPS remains a formidable challenge, both theoreti-
 41 cally and computationally. On the theoretical side, the thermo-chemical reactions, coupled
 42 with the irregular pore network structure and ablating boundaries, translate into complex
 43 non-linear equations governing multi-physical interactions across several spatio-temporal
 44 scales [1, 8]. On the computational side, numerical approaches based on finite-element
 45 (FEM) or finite-volume (FVM) methods yield systems of differential equations modeling the
 46 transient thermo-ablative response of the TPS [5]. The FEM discretizations lead to high-
 47 dimensional systems of equations, resulting in prohibitive computational costs for many-
 48 query applications such as design, optimization, uncertainty quantification, and real-time
 49 applications, where possibly thousands of model evaluations are required.

50 Reduced-order models (ROMs) have emerged as a promising approach to alleviate the
 51 computational costs of high-fidelity simulations [6, 11]. Ideally, a ROM should be: (1)
 52 accurate to reproduce high-fidelity solutions, (2) support continuous or infinite-dimensional
 53 design parameters such as geometrical shapes and material distributions, (3) be computa-
 54 tionally efficient to evaluate to allow for fast turnaround times in design optimization. However,
 55 the above three capabilities usually form an *impossible trinity of modeling*, as illustrated in
 56 Fig. 1; building a ROM that achieves any two capabilities sacrifices the third.

57 The impossible trinity poses a significant challenge in the development of ROMs for
 58 the multi-disciplinary transient analysis and optimization of ablating TPS. Specifically, full-
 59 order models (FOMs), e.g., FEMs or FVMs, offer high accuracy and robust generalization
 60 over design spaces, but are computationally expensive to evaluate. Reduced-physics models
 61 (RPMs) – such as simplified convective-radiative heat transfer or engineering correlations –
 62 are low-dimensional models that achieve efficiency and broad applicability by ignoring higher-
 63 order non-linear effects. However, RPMs sacrifice accuracy for complex thermo-ablative
 64 responses due to the simplifications and assumptions inherent in their formulation, and it
 65 is generally not clear how to systematically leverage existing high-fidelity data to improve
 66 RPMs [19].

67 Lastly, data-driven ROMs, such as Gaussian Process Regression (GPR) [16], Neural Net-
68 works (NNs), and neural ordinary differential equations (NODEs) [3], can provide accurate
69 and computationally-efficient approximations of high-fidelity models for complex thermo-
70 ablative responses. However, these data-centric approaches often demand extensive high-
71 fidelity data for training, do not necessarily satisfy fundamental physical constraints or con-
72 servation laws, and thus do not generalize well to the design spaces outside the training [17].
73 For example, our previous work demonstrated that NODEs trained on high-fidelity data of
74 non-ablating TPS failed to generalize when subjected to boundary conditions and material
75 models outside the training set [18].

76 This work presents the extension of the *physics-infused reduced-order modeling* (PIROM)
77 framework to include effects of ablation for TPS applications, previously ignored in Ref. [18].
78 Specifically, the PIROM is demonstrated for the transient thermo-ablative response of multi-
79 layered hypersonic TPS. The PIROM is a non-intrusive framework that combines the strengths
80 of physics-based models with machine learning to formulate and train ROMs for parametrized
81 non-linear dynamical systems. The backbone of the PIROM is the physics-based component,
82 i.e., the RPM, which in this work is composed of: (1) a *lumped capacitance model* (LCM)
83 to model the average heat transfer within the TPS layers, and (2) a *surface recession model*
84 (SRM) to model one-dimensional surface ablation.

85 Leveraging the *Mori-Zwanzig* (MZ) formalism [15, 14, 13], the RPM is rigorously ex-
86 tended with data-driven hidden dynamics to account for the missing physics in the LCM,
87 which are learned from high-fidelity data. The hidden dynamics enable higher predictive
88 accuracy of the PIROM when subjected to complex boundary conditions and SRM model
89 variations. For the TPS problem, the MZ approach produces a sufficiently simple model
90 form while maintaining the physical consistency of the PIROM, as well as the dependence
91 on design parameters. Thus, the PIROM aims to solve the ITM by leveraging the gen-
92 eralizability and computational efficiency of RPMs, while incorporating the accuracy and
93 adaptability of data-driven extensions. More importantly, the PIROM formulation provides
94 a general methodology for developing PIROMs for other multi-physics problems.

95 The specific objectives of this work are summarized as follows:

- 96 1. Extend the previous PIROM formulation in Ref. [18] to model transient thermo-
97 ablative response of multi-layered hypersonic TPS through a systematic coarse-graining
98 procedure based on the Mori-Zwanzig formalism.
- 99 2. Benchmark the accuracy, generalizability, and computational accelerations of the PIROM
100 against the RPM and the high-fidelity FEM solutions of ablating TPS, thus quanti-
101 fying the PIROM’s capabilities to solve the ITM in complex multi-physical non-linear
102 dynamical systems.

103 2 Modeling of Thermal Protection Systems

104 This section presents the problem of modeling the transient thermo-ablative response of a
105 non-decomposing TPS, subjected to extreme hypersonic heating. Two different but math-
106 ematically connected solution strategies are provided: (1) a high-fidelity full-order model

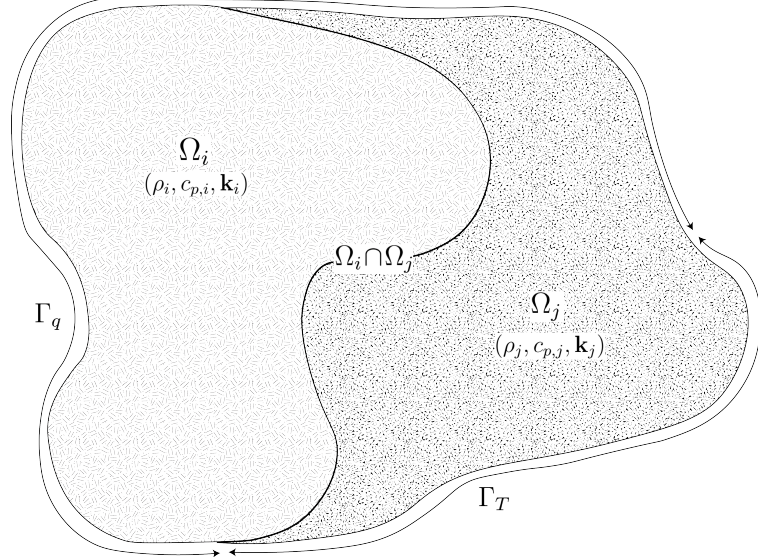


Figure 2: General domain Ω with prescribed Neumann and Dirichlet boundary conditions on Γ_q and Γ_T . Mesh displacement $w(x, t)$ occurs on the Γ_q boundary.

107 (FOM) based on a finite element method (FEM), and (2) a RPM based on a *lumped capacitance model* (LCM) coupled with a one-dimensional *surface recession model* (SRM). The
108 FOM is computationally expensive but provides the highest fidelity, while the RPM is com-
109 putationally efficient but has low predictive fidelity. However, both models are physically
110 consistent to high-dimensional design variables. The following discussion presents the TPS
111 modeling problem and the FOM and RPM solution strategies.
112

113 2.1 Governing Equations

114 The multi-physics of a non-decomposing ablating TPS under a hypersonic boundary layer
115 involves the *energy equation* for heat conduction inside the TPS, and the *pseudo-elasticity*
116 *equation* for mesh motion due to surface recession. The coupling between these two equations
117 occurs at the heated boundary, where the surface temperature drives the surface recession
118 velocity, which appears as an advection term in the energy equation. The governing PDEs
119 are described as follows.

120 2.1.1 Energy Equation

121 Consider a generic domain $\Omega \subset \mathbb{R}^d$, $d = 2$ or 3 , illustrated in Fig. 2. Let $\partial\Omega = \Gamma_q \cup \Gamma_T$
122 and $\Gamma_q \cap \Gamma_T = \emptyset$, where a Neumann $q_b(x, t)$ boundary condition is prescribed on the heated
123 boundary Γ_q , and represents the surface exposed to the hypersonic boundary layer. The
124 Dirichlet $T_b(x, t)$ boundary condition is prescribed on the boundary Γ_T . The TPS is divided
125 into N non-overlapping components $\{\Omega_i\}_{i=1}^N$, as illustrated in Fig. 2 for $N = 2$. The i -th
126 component Ω_i is associated with material properties $(\rho_i, c_{p,i}, \mathbf{k}_i)$, which are continuous within
127 one component, and can be discontinuous across two neighboring components.

¹²⁸ The energy equation describes the transient heat conduction,

$$\rho c_p \left(\frac{\partial T}{\partial t} + \tilde{\mathbf{v}}(x, t) \cdot \nabla T \right) - \nabla \cdot (\mathbf{k} \nabla T) = 0, \quad x \in \Omega \quad (1a)$$

$$-\mathbf{k} \nabla T \cdot \mathbf{n} = q_b(x, t), \quad x \in \Gamma_q \quad (1b)$$

$$T(x, t) = T_b(x, t), \quad x \in \Gamma_T \quad (1c)$$

$$T(x, 0) = T_0(x), \quad x \in \Omega \quad (1d)$$

¹²⁹ where ρ , c_p , and $\mathbf{k} \in \mathbb{R}^{d \times d}$ are the constant density, heat capacity, and thermal conductivity.
¹³⁰ Note that our prior work has applied the PIROM to TPS problems with temperature-varying
¹³¹ material properties [18]. In the order they appear, the $\rho c_p \frac{\partial T}{\partial t}$ term includes the unsteady
¹³² energy storage, $\rho c_p \tilde{\mathbf{v}}(x, t) \cdot \nabla T$ includes the temperature advection due to ablation, and
¹³³ $\nabla \cdot (\mathbf{k} \nabla T)$ includes the heat conduction.

¹³⁴ An Arbitrary Lagrangian-Eulerian (ALE) description is used to account for mesh motion
¹³⁵ due to surface recession. The relative velocity of the material $\tilde{\mathbf{v}}(x, t)$ with respect to the
¹³⁶ mesh is,

$$\tilde{\mathbf{v}}(x, t) = \mathbf{v}_s(x, t) - \mathbf{v}_m(x, t) \quad (2)$$

¹³⁷ where $\mathbf{v}_s(x, t)$ and $\mathbf{v}_m(x, t)$ are the physical material velocity and mesh velocity, respectively.
¹³⁸ In this work, the physical material velocity is assumed to be zero, i.e., $\mathbf{v}_s(x, t) = \mathbf{0}$, and thus
¹³⁹ the relative velocity is simply the negative of the mesh velocity, $\tilde{\mathbf{v}}(x, t) = -\mathbf{v}_m(x, t)$.

¹⁴⁰ 2.1.2 Pseudo-Elasticity Equation

¹⁴¹ The mesh displacements $\mathbf{d} \in \mathbb{R}^d$ are described by the steady-state pseudo-elasticity equation,
¹⁴² which models the mesh as a fictitious elastic solid that deforms according to the prescribed
¹⁴³ boundary displacements. The governing equation is given as,

$$\nabla \cdot \boldsymbol{\sigma}(\mathbf{d}) = \mathbf{0}, \quad \forall t \in \mathcal{T}, \quad x \in \Omega \quad (3a)$$

$$\mathbf{d}(x, t) = \mathbf{d}_q(x, t), \quad \forall t \in \mathcal{T}, \quad x \in \Gamma_q \quad (3b)$$

$$\mathbf{d}(x, t) = \mathbf{0}, \quad \forall t \in \mathcal{T}, \quad x \in \Gamma_T \quad (3c)$$

$$\mathbf{d}(x, 0) = \mathbf{0}, \quad \forall x \in \Omega \quad (3d)$$

¹⁴⁴ where the stress tensor $\boldsymbol{\sigma}$ is related to the strain tensor $\boldsymbol{\epsilon}(\mathbf{d})$ through Hooke's law,

$$\boldsymbol{\sigma}(\mathbf{d}) = \mathbb{D} : \boldsymbol{\epsilon}(\mathbf{d})$$

¹⁴⁵ where \mathbb{D} is the fourth-order positive definite elasticity tensor, and “ $:$ ” is the double con-
¹⁴⁶ traction of the full-order tensor \mathbb{D} with the second-order tensor $\boldsymbol{\epsilon}$. The elasticity tensor
¹⁴⁷ ordinarily possess a number of symmetries, effectively reducing the number of components
¹⁴⁸ that describe it [2]. In this work, the standard isotropic case with rotational symmetry is
¹⁴⁹ considered, where \mathbb{D} is fully described by two Lamé parameters λ and μ arbitrarily chosen
¹⁵⁰ to tailor the mesh deformation. The symmetric strain tensor $\boldsymbol{\epsilon}$ measures the deformation of

151 the mesh due to displacements $\mathbf{d}(x, t)$, and is defined as,

$$\boldsymbol{\epsilon}(\mathbf{d}) = \frac{1}{2} (\nabla \mathbf{d} + \nabla \mathbf{d}^\top)$$

152 The “material” properties for the mesh are chosen to tailor the mesh deformation, and need
153 not represent the actual material being modeled [1].

154 For the pseudo-elasticity equations, the boundary conditions include prescribed displace-
155 ments $\mathbf{d}_q(x, t)$ on the heated boundary Γ_q in eq. (3b), and zero displacements on the unheated
156 boundaries in eq. (3c). The initial condition for the mesh displacements is zero in eq. (3d).
157 Particularly, the surface velocity due to the ablating material is a function of the surface
158 temperature $T_q(x, t)$ for $x \in \Gamma_q$ on the heated boundary. For the i -th material component,
159 the mesh velocity on the heated boundary is imposed based on the following relation,

$$\hat{\mathbf{n}} \cdot \mathbf{v}_m(x, t) = f_i(T_q(x, t)), \quad x \in \Gamma_{q,i} \quad (4)$$

160 where $\Gamma_q = \cup_{i=1}^{\tilde{N}} \Gamma_{q,i}$ with $\Gamma_{q,i}$ as the portion of the heated boundary that belongs to the
161 i -th ablative component, \tilde{N} is the number of ablative components with $\tilde{N} \leq N$, $\hat{\mathbf{n}}$ is the
162 unit normal vector, and f_i is a material-dependent function obtained from tabulated data,
163 commonly referred to as a B’ table [1]. The B’ table provides a model for the recession
164 velocity as a function of the surface temperature, and is pre-computed based on high-fidelity
165 simulations or physical experiments for a one-dimensional slab of materials, and is indepen-
166 dent of the TPS geometry. Provided the surface velocity, the boundary condition in eq. (5)
167 for the mesh displacements are computed by integrating the surface velocity over time,

$$\mathbf{d}_q(x, t) = \int_0^t \mathbf{v}_m(x, \tau) d\tau \quad (5)$$

168 2.2 Full-Order Model: Finite-Element Method

169 The following discussion presents the high-fidelity transient thermo-ablative modeling of the
170 TPS as the FOM. Specifically, the FOM is based on *finite-element methods* (FEM) for the
171 governing PDEs in eq. (1), and is implemented in the SIERRA/Aria code developed at
172 Sandia National Laboratories [2]. A *Discontinuous Galerkin FEM* (DG-FEM) method is
173 used to spatially discretize the energy equation for theoretical convenience, while a standard
174 Galerkin FEM is used to spatially discretize the pseudo-elasticity equation for mesh motion.
175 The following discussion presents the spatial discretization of both governing equations.

176 **Energy Equation** To obtain the full-order numerical solution, the *energy equation* is spa-
177 tially discretized using variational principles of DG-FEM [5]. Note that the choice of DG
178 approach is mainly for theoretical convenience, and is exclusively performed on the energy
179 equation, as it is the surface temperature that drives the ablation process; the equivalence be-
180 tween DG and FEM is noted upon their convergence. Consider a conforming mesh partition
181 domain, where each element belongs to one and only one component. Denote the collection
182 of all M elements as $\{E_i\}_{i=1}^M$. In an element E_i , its shared boundaries with another element
183 E_j , Neumann BC, and Dirichlet BC are denoted as e_{ij} , e_{iq} , and e_{iT} , respectively. Lastly,

¹⁸⁴ $|e|$ denotes the length ($n_d = 2$) or area ($n_d = 3$) of a component boundary e . For the i -th
¹⁸⁵ element, use a set of P trial functions, such as polynomials, to represent the temperature
¹⁸⁶ distribution,

$$T_i(x, t) = \sum_{l=1}^P \phi_l^i(x) u_l^i(t) \equiv \phi_i^\top(x) \mathbf{u}_i(t), \quad i = 1, 2, \dots, M \quad (6)$$

¹⁸⁷ Then, the energy equation is collected into a block-system of ODEs for all the elements in
¹⁸⁸ the mesh,

$$\mathbf{A}\dot{\mathbf{u}} = [\mathbf{B} + \mathbf{C}(\mathbf{u})] \mathbf{u} + \mathbf{f}(t) \quad (7)$$

¹⁸⁹ where $\mathbf{u} = [\mathbf{u}_1, \mathbf{u}_2, \dots, \mathbf{u}_M]^\top \in \mathbb{R}^{MP}$ includes all the DG variables, $\mathbf{f} \in \mathbb{R}^{MP}$ is the external
¹⁹⁰ forcing, and the system matrices \mathbf{A} , \mathbf{B} , and \mathbf{C} are the matrices due to heat capacity, heat
¹⁹¹ conduction, and temperature advection due to mesh motion, respectively. Note that the
¹⁹² advection matrix $\mathbf{C}(\mathbf{u})$ is a function of the temperature \mathbf{u} since it depends on the mesh
¹⁹³ velocity as in eq. (4); this is the main source of non-linearity in the current TPS problem.
¹⁹⁴ A detailed derivation of eq. (7) and their matrices is provided in Appendix A.

¹⁹⁵ **Pseudo-Elasticity Equation** The *pseudo-elasticity equation* is spatially discretized us-
¹⁹⁶ ing the standard Galerkin FEM method on a structured mesh with quadrilateral elements.
¹⁹⁷ Define the scalar basis functions $\{\psi_q(x)\}_{q=1}^Q$ nodal variables $\{\mathbf{d}_q\}_{q=1}^Q$ for the mesh displace-
¹⁹⁸ ments, where Q is the number of basis functions. Express the mesh displacements \mathbf{w} at time
¹⁹⁹ t as,

$$\mathbf{w}(x, t) \approx \sum_{q=1}^Q \psi_q(x) \mathbf{w}_q \quad (8)$$

²⁰⁰ Substituting into the Galerkin weak form of the *steady* pseudo-elasticity equation, the fol-
²⁰¹ lowing linear system of equations is obtained for the nodal displacements,

$$\mathbf{K}\mathbf{w} = \mathbf{g} \quad (9)$$

²⁰² where \mathbf{w} is the global displacement vector, $\mathbf{K} \in \mathbb{R}^{dQ \times dQ}$ the global stiffness matrix of dimen-
²⁰³ sion d , defined by the volume integrals over the domain Ω provided the elasticity tensor \mathbb{D} ,
²⁰⁴ and \mathbf{g} is the global force vector due to the Dirichlet boundary conditions on the heated Γ_q
²⁰⁵ and unheated Γ_T boundaries.

²⁰⁶ 2.3 Reduced-Physics Model

²⁰⁷ The RPM for predicting the response of the ablating TPS consists of two components: (1)
²⁰⁸ *surface recession model* (SRM) and a *lumped capacitance model* (LCM). The SRM provides
²⁰⁹ a relation between the surface temperature and *one-dimensional* surface recession veloc-
²¹⁰ ity based on pre-computed B' tables for the material, enabling the computation of *one-*
²¹¹ *dimensional* surface displacements. Provided the geometry changed induced by the surface
²¹² recession, the LCM predicts the average temperature inside each component of the TPS,
²¹³ which are in turn used as low-fidelity estimates for the surface temperatures required by the
²¹⁴ SRM. Therefore, the SRM and LCM are coupled to define the RPM, providing low-fidelity
²¹⁵ estimates for temperatures and surface recessions of the ablating TPS.

²¹⁶ **2.3.1 Surface Recession Model**

²¹⁷ The mesh displacements \mathbf{d} are constrained to be *one-dimensional* on the heated boundary
²¹⁸ Γ_q , i.e., $w_i(x, t) = \mathbf{d}(x, t) \cdot \hat{\mathbf{n}}$, where $\hat{\mathbf{n}}$ is the unit normal vector on the heated bound-
²¹⁹ ary Γ_q . Displacements perpendicular to $\hat{\mathbf{n}}$ are assumed small and are neglected. Let
²²⁰ $\mathbf{w} = [w_1, w_2, \dots, w_{\tilde{N}}]^\top \in \mathbb{R}^{\tilde{N}}$ include the one-dimensional displacements for the \tilde{N} ablat-
²²¹ ing components on the heated boundary, where $\tilde{N} \leq N$. Then the SRM is described as,

$$\dot{\mathbf{w}} = \boldsymbol{\Xi}\mathbf{u} - \tilde{\mathbf{f}} \quad (10)$$

²²² where $\boldsymbol{\Xi} = \text{diag}(\alpha_1, \dots, \alpha_{\tilde{N}})$ and $\tilde{\mathbf{f}} = (\alpha_1 u_{0,1}, \dots, \alpha_{\tilde{N}} u_{0,\tilde{N}})^\top$. The constants α_i are small
²²³ material-dependent parameters, determined from the B' table, and $u_{0,i}$ is the constant initial
²²⁴ temperature of the ablative component. The SRM provides a relation between the surface's
²²⁵ temperature and recession velocity, based on pre-computed B' tables for the material.

²²⁶ **2.3.2 Lumped Capacitance Model**

²²⁷ A general form of the LCM is provided in this section; details regarding the derivation for
²²⁸ the four-component TPS used in the results section are provided in Appendix A. Let Ω be
²²⁹ partitioned into N non-overlapping components $\{\Omega_i\}_{i=1}^N$, as illustrated in Fig. 2 for $N = 2$.
²³⁰ The domain Ω is a function of the surface displacements \mathbf{w} , and thus the geometry of each
²³¹ component Ω_i is time-dependent. The LCM predicts the temporal variation of average
²³² temperatures in multiple shape-varying interconnected components [9]. From a point of
²³³ view of energy conservation, the LCM leads to the following system of first-order ODEs for
²³⁴ the average temperatures in the components,

$$\bar{\mathbf{A}}(\mathbf{w})\dot{\bar{\mathbf{u}}} = \bar{\mathbf{B}}(\mathbf{w})\bar{\mathbf{u}} + \bar{\mathbf{f}}(t) \quad (11)$$

²³⁵ Where the states and inputs,

$$\bar{\mathbf{u}} = [\bar{u}_1, \bar{u}_2, \dots, \bar{u}_N]^\top \in \mathbb{R}^N, \quad \bar{\mathbf{f}} = [\bar{f}_1, \bar{f}_2, \dots, \bar{f}_N]^\top \in \mathbb{R}^N \quad (12)$$

²³⁶ include the average temperatures $\bar{\mathbf{u}}$ and spatially-integrated inputs $\bar{\mathbf{f}}$ for the N components.
²³⁷ For $i, j = 1, 2, \dots, N$ the (i, j) -th elements of the $\bar{\mathbf{A}} \in \mathbb{R}^{N \times N}$, $\bar{\mathbf{B}} \in \mathbb{R}^{N \times N}$, and $\bar{\mathbf{f}} \in \mathbb{R}^N$
²³⁸ matrices are given by,

$$\bar{A}_i = \begin{cases} \int_{\Omega_i} \rho c_p d\Omega_i, & i = j \\ 0, & i \neq j \end{cases}, \quad \bar{B}_{ij} = \begin{cases} \sum_{j \in \mathcal{N}_i \cup \{T_b\}} \bar{B}_{ij}^i, & i = j \\ \bar{B}_{ij}^{(j)}, & i \neq j \end{cases}, \quad (13a)$$

$$\mathbf{f}_i = \begin{cases} |e_{iq}| \bar{q}_i + \frac{|e_{iT}|}{R_i} \bar{T}_i, & i = j \\ 0, & i \neq j \end{cases} \quad (13b)$$

²³⁹ where,

$$\bar{q}_i = \frac{1}{|e_{iq}|} \int_{e_{iq}} q_b d e_{iq}, \quad \bar{T}_i = \frac{1}{|e_{iT}|} \int_{e_{iT}} T_b d e_{iT}, \quad \bar{B}_{ij}^i = -\frac{|e_{ij}|}{R_{ij}}, \quad \bar{B}_{ij}^j = \frac{|e_{ij}|}{R_{ij}} \quad (14)$$

240 where R_{ij} is the equivalent thermal resistance between two neighboring components Ω_i and
 241 Ω_j , and R_i is the thermal resistance between component Ω_i and the Dirichlet boundary.
 242 Note that the heat capacitances and thermal resistances are computed based on the current
 243 geometry of each component, which is a function of \mathbf{w} provided by the SRM.

244 2.3.3 Thermo-Ablative Reduced-Physics Model

245 The SRM and LCM are combined to define the RPM for predicting the thermo-ablative
 246 response of the TPS under hypersonic boundary layers. Specifically, the RPM is defined as
 247 the LCM as in eq. (11), where the *geometry-dependent* matrices $\bar{\mathbf{A}}$ and $\bar{\mathbf{B}}$ are updated at
 248 each time step based on the current displacements \mathbf{w} provided by the SRM. The RPM is
 249 formally stated as,

$$\tilde{\mathbf{A}}(\mathbf{s})\dot{\mathbf{s}} = \tilde{\mathbf{B}}(\mathbf{s})\mathbf{s} + \tilde{\mathbf{F}}(t) \quad (15a)$$

$$\tilde{\mathbf{z}} = \mathbf{s} \quad (15b)$$

250 where the state $\mathbf{s} = [\bar{\mathbf{u}}, \mathbf{w}]^\top \in \mathbb{R}^{N+\tilde{N}}$ includes the *average temperature* and *one-dimensional*
 251 *surface displacements*, and \tilde{N} is the number of ablating components with $\tilde{N} \leq N$. Moreover,
 252 the observables are defined as $\mathbf{z} = [\bar{\mathbf{u}}, \mathbf{w}]^\top \in \mathbb{R}^{N+\tilde{N}}$. The matrices are given as,

$$\tilde{\mathbf{A}}(\mathbf{s}) = \begin{bmatrix} \bar{\mathbf{A}}(\mathbf{s}) & \mathbf{0} \\ \mathbf{0} & \mathbf{I} \end{bmatrix}, \quad \tilde{\mathbf{B}}(\mathbf{s}) = \begin{bmatrix} \bar{\mathbf{B}}(\mathbf{s}) & \mathbf{0} \\ \Xi & \mathbf{0} \end{bmatrix}, \quad \tilde{\mathbf{F}}(t) = \begin{bmatrix} \bar{\mathbf{f}}(t) \\ -\tilde{\mathbf{f}} \end{bmatrix} \quad (16)$$

253 In the matrices $\tilde{\mathbf{A}}$ and $\tilde{\mathbf{B}}$, the surface displacements \mathbf{w} are used to define the dimensions for
 254 the Ω_i component used in eqs. (13) and (14), thus effectively coupling the LCM and SRM.

255 2.4 Summary of Modeling Approaches

256 The FOM (i.e., FEM) and RPM (i.e., LCM with SRM) are two different but mathematically
 257 connected solution strategies. Particularly, the LCM in eq. (11) not only resembles the
 258 functional form of the DG model in eq. (7), but can be viewed as a special case of the latter,
 259 where the mesh partition is extremely coarse, and the trial and test functions are piece-wise
 260 constants. This removes all spatial variations within each component, and neglects advection
 261 effects due to mesh motion.

262 For example, consider the case where each component Ω_i is treated as one single element,
 263 and each element employs one constant basis function $\phi_i = 1$. The DG-FEM model for the
 264 i -th component simplifies to the scalar ODE,

$$\mathbf{A}^{(i)} = \bar{A}_i, \quad \mathbf{C}^{(i)} = 0, \quad \mathbf{B}_{ij}^{(i)} = -\sigma|e_{ij}|, \quad \mathbf{B}_{ij}^{(j)} = \sigma|e_{ij}|, \quad \mathbf{f}_i = |e_{iq}|\bar{q}_i + \sigma|e_{iT}|\bar{T}_i \quad (17)$$

265 Clearly, the LCM is a coarse zeroth-order DG model with the inverse of thermal resistance
 266 chosen as the element-wise penalty factors. Or conversely, the DG model is a refined version
 267 of LCM via *hp*-adaptation.

268 The FOM and RPM represent two extremes in the modeling fidelity and computational
 269 cost spectrum. On one hand, the FOM is the most accurate but computationally expensive

270 to evaluate due to the fine mesh discretizations for both the temperature and displacement
 271 fields, leading to possibly millions of state variables. On the other hand, the RPM considers
 272 only the average temperature of the material, from which the displacements are obtained by
 273 integrating the velocity. The coarsened representation of the temperature field significantly
 274 reduces the number of state variables to only a few per component, and thus reducing the
 275 computational cost. However, this sacrifices local temperature information that becomes
 276 critical to properly capture higher-order effects due to mesh motion and thermal gradients
 277 within each component. Thus, neither the FOM nor the RPM is an universal approach for
 278 real-world analysis, design, and optimization tasks for ablating TPS, where thousands of
 279 high-fidelity model evaluations may be necessary. This issue motivates the development of
 280 the PIROM, which can achieve the fidelity of FOM at a computational cost close to the
 281 RPM, while maintaining the generalizability to model parameters.

282 3 Physics-Infused Reduced-Order Modeling

283 The formulation of PIROM for ablating TPS starts by connecting the FOM, i.e., the DG-
 284 FEM, and the RPM, i.e., the LCM, via a coarse-graining procedure. This procedure pin-
 285 points the missing dynamics in the LCM when compared to DG-FEM. Subsequently, the
 286 Mori-Zwanzig (MZ) formalism is employed to determine the model form for the missing dy-
 287 namics in PIROM. Lastly, the data-driven identification of the missing dynamics in PIROM
 288 is presented.

289 3.1 Deriving the Reduced-Physics Model via Coarse-Graining

290 The subsequent coarse-graining formulation is performed on the DG-FEM in eq. (7) to
 291 derive the LCM in eq. (11). This process constraints the trial function space of a full-
 292 order DG model to a subset of piece-wise constants, so that the variables \mathbf{u} , matrices \mathbf{A} ,
 293 \mathbf{B} , and \mathbf{C} , and forcing vector \mathbf{f} are all approximated using a single state associated to the
 294 average temperature. Note that the coarse-graining is exclusively performed on the thermal
 295 dynamics, as it is the surface temperature that drives the one-dimensional recession via
 296 the SRM. Hence, the coarse-graining of the mesh dynamics is not included in the following
 297 procedure.

298 3.1.1 Coarse-Graining of States

299 Consider a DG model as in eq. (7) for M elements and an LCM as in eq. (11) for N compo-
 300 nents; clearly $M \gg N$. Let $\mathcal{V}_j = \{i | E_i \in \Omega_j\}$ be the indices of the elements belonging to the
 301 j -th component, so $E_i \in \Omega_j$ for all $i \in \mathcal{V}_j$. The number of elements in the j -th component is
 302 $|\mathcal{V}_j|$. The average temperature on Ω_j is,

$$303 \bar{u}_j = \frac{1}{|\Omega_j|} \sum_{i \in \mathcal{V}_j} \int_{E_i} \phi^{(i)}(x)^T \mathbf{u}^{(i)} d\Omega = \frac{1}{|\Omega_j|} \sum_{i \in \mathcal{V}_j} |E_i| \boldsymbol{\varphi}_i^{j\top} \mathbf{u}^{(i)}, \quad j = 1, 2, \dots, N \quad (18)$$

303 where $|\Omega_j|$ and $|E_i|$ denote the area ($d = 2$) or volume ($d = 3$) of component j and element
 304 i , respectively. The orthogonal basis functions are defined as $\varphi_i^{j\top} = [1, 0, \dots, 0]^\top \in \mathbb{R}^P$.

305 Conversely, given the average temperatures of the N components, $\bar{\mathbf{u}}$, the states of an
 306 arbitrary element E_i is written as,

$$\mathbf{u}^{(i)} = \sum_{k=1}^N \varphi_i^k \bar{u}_k + \delta \mathbf{u}^{(i)}, \quad i = 1, 2, \dots, M \quad (19)$$

307 where $\varphi_i^k = 0$ if $i \notin \mathcal{V}_k$, and $\delta \mathbf{u}^{(i)}$ represents the deviation from the average temperature and
 308 satisfies the orthogonality condition $\varphi_i^{k\top} \delta \mathbf{u}^{(i)} = 0$ for all k .

309 Equations eqs. (18) and (19) are combined and written in matrix form as,

$$\bar{\mathbf{u}} = \Phi^+ \mathbf{u}, \quad \mathbf{u} = \Phi \mathbf{u} + \delta \mathbf{u} \quad (20)$$

310 where $\Phi \in \mathbb{R}^{MP \times N}$ is a matrix of $M \times N$ blocks, with the (i, j) -th block as φ_i^j , $\Phi^+ \in \mathbb{R}^{N \times MP}$
 311 is the left inverse of Φ , with the (i, j) -th block as $\varphi_i^{j+} = \frac{|E_i|}{|\Omega_j|} \varphi_i^{j\top}$, and $\delta \mathbf{u}$ is the collection of
 312 deviations. By their definitions, $\Phi^+ \Phi = \mathbf{I}$ and $\Phi^+ \delta \mathbf{u} = \mathbf{0}$.

313 3.1.2 Coarse-Graining of Dynamics

314 The dependence of the matrices with respect to the displacements \mathbf{w} is dropped to isolate
 315 the analysis based on coarsened variables. Consider a function of states in the form of
 316 $\mathbf{M}(\mathbf{u})\mathbf{g}(\mathbf{u})$, where $\mathbf{g} : \mathbb{R}^{MP} \rightarrow \mathbb{R}^{MP}$ is a vector-valued function, and $\mathbf{M} : \mathbb{R}^{MP} \rightarrow \mathbb{R}^{p \times MP}$
 317 is a matrix-valued function with an arbitrary dimension p . Define the projection matrix
 318 $\mathbf{P} = \Phi \Phi^+$ and the projection operator \mathcal{P} as,

$$\begin{aligned} \mathcal{P} [\mathbf{M}(\mathbf{u})\mathbf{g}(\mathbf{u})] &= \mathbf{M}(\mathbf{P}\mathbf{u})\mathbf{g}(\mathbf{P}\mathbf{u}) \\ &= \mathbf{M}(\Phi\bar{\mathbf{u}})\mathbf{g}(\Phi\bar{\mathbf{u}}) \end{aligned} \quad (21)$$

319 so that the resulting function depends only on the average temperatures $\bar{\mathbf{u}}$. Correspondingly,
 320 the residual operator $\mathcal{Q} = \mathcal{I} - \mathcal{P}$, and $\mathcal{Q}[\mathbf{M}(\mathbf{u})\mathbf{g}(\mathbf{u})] = \mathbf{M}(\mathbf{u})\mathbf{g}(\mathbf{u}) - \mathbf{M}(\Phi\bar{\mathbf{u}})\mathbf{g}(\Phi\bar{\mathbf{u}})$. When
 321 the function is not separable, the projection operator is simply defined as $\mathcal{P}[\mathbf{g}(\mathbf{u})] = \mathbf{g}(\mathbf{P}\mathbf{u})$.

322 Subsequently, the operators defined above are applied to coarse-grain the dynamics. First,
 323 write the DG-FEM in eq. (7) as,

$$\dot{\mathbf{u}} = \mathbf{A}^{-1} \mathbf{B} \mathbf{u} + \mathbf{A}^{-1} \mathbf{C}(\mathbf{u}) \mathbf{u} + \mathbf{A}^{-1} \mathbf{f}(t) \quad (22)$$

324 and multiply both sides by Φ^+ to obtain,

$$\Phi^+ \dot{\mathbf{u}} = \Phi^+ (\Phi \dot{\bar{\mathbf{u}}} + \delta \dot{\mathbf{u}}) = \dot{\bar{\mathbf{u}}} = \Phi^+ \mathbf{r}(\mathbf{u}, t) \quad (23)$$

325 Apply the projection operator \mathcal{P} and the residual operator \mathcal{Q} to the right-hand side to obtain,

$$\dot{\bar{\mathbf{u}}} = \mathcal{P} [\Phi^+ \mathbf{r}(\mathbf{u}, t)] + \mathcal{Q} [\Phi^+ \mathbf{r}(\mathbf{u}, t)] \equiv \mathbf{r}^{(1)}(\bar{\mathbf{u}}, t) + \mathbf{r}^{(2)}(\mathbf{u}, t) \quad (24)$$

326 where $\mathbf{r}^{(1)}(\bar{\mathbf{u}}, t)$ is resolved dynamics that depends on $\bar{\mathbf{u}}$ only, and $\mathbf{r}^{(2)}(\mathbf{u}, t)$ is the un-resolved

327 or residual dynamics. Detailed derivations and analysis of $\mathbf{r}^{(1)}(\bar{\mathbf{u}}, t)$ and $\mathbf{r}^{(2)}(\mathbf{u}, t)$ can be
328 found in the Appendix.

329 It follows from our previous work in Ref. [18] that the resolved dynamics is exactly the
330 LCM, where the advection term reduces to zero, i.e., $\bar{\mathbf{C}}(\bar{\mathbf{u}}) = \mathbf{0}$, as shown in the Appendix.
331 Using the notation from eq. (11), it follows that,

$$\begin{aligned}\mathbf{r}^{(1)}(\bar{\mathbf{u}}, t) &= \bar{\mathbf{A}}(\mathbf{w})^{-1}\bar{\mathbf{B}}(\mathbf{w})\bar{\mathbf{u}} + \bar{\mathbf{A}}(\mathbf{w})^{-1}\bar{\mathbf{C}}(\bar{\mathbf{u}})\bar{\mathbf{u}} + \bar{\mathbf{A}}(\mathbf{w})^{-1}\bar{\mathbf{f}}(\bar{\mathbf{u}}) \\ &= \bar{\mathbf{A}}(\mathbf{w})^{-1}\bar{\mathbf{B}}(\mathbf{w})\bar{\mathbf{u}} + \bar{\mathbf{A}}(\mathbf{w})^{-1}\bar{\mathbf{f}}(t)\end{aligned}\quad (25)$$

332 where the following relations hold,

$$\bar{\mathbf{A}}(\mathbf{w}) = \mathbf{W} (\Phi^+ \mathbf{A}^{-1} \Phi)^{-1} \quad (26a)$$

$$\bar{\mathbf{B}}(\mathbf{w}) = \mathbf{W} \Phi^+ \mathbf{B} \Phi \quad (26b)$$

333 where $\mathbf{W} \in \mathbb{R}^{N \times N}$ is a diagonal matrix with the i -th element as $[\mathbf{W}]_{ii} = |\mathcal{V}_k|$ if $i \in \mathcal{V}_k$.
334 The examination of the second residual term $\mathbf{r}^{(2)}(\mathbf{u}, t)$ in eq. (24) is shown in the Appendix,
335 and demonstrates that the physical sources of missing dynamics in the LCM include: the
336 approximation of non-uniform temperature within each component as a constant, and the
337 elimination of the advection term due to coarse-graining. In sum, the above along with the
338 derivations in the Appendix not only show that the LCM is a result of coarse-graining of
339 the full-order DG-FEM, but also reveal the discrepancies between the LCM and the DG-
340 FEM. These discrepancies propagate into the SRM, which as a result of the averaging in the
341 LCM formulation, under-predicts the surface recession rates. In the subsequent section, the
342 discrepancies in the LCM are corrected to formulate the PIROM.

343 3.2 Physics-Infusion Via Mori-Zwanzig Formalism

344 The Mori-Zwanzig (MZ) formalism is an operator-projection technique used to derive ROMs
345 for high-dimensional dynamical systems, especially in statistical mechanics and fluid dy-
346 namics [13, 14, 15]. It provides an exact reformulation of a high-dimensional Markovian dy-
347 namical system, into a low-dimensional observable non-Markovian dynamical system. The
348 proposed ROM is subsequently developed based on the approximation to the non-Markovian
349 term in the observable dynamics. Particularly, eq. (24) shows that the DG-FEM dynam-
350 ics can be decomposed into the resolved dynamics $\mathbf{r}^{(1)}(\bar{\mathbf{u}}, t)$ and the orthogonal dynamics
351 $\mathbf{r}^{(2)}(\mathbf{u}, t)$, in the sense of $\mathcal{P}\mathbf{r}^{(2)} = 0$. In this case, the MZ formalism can be invoked to ex-
352 press the dynamics $\bar{\mathbf{u}}$ in terms of $\bar{\mathbf{u}}$ alone as the projected Generalized Langevin Equation
353 (GLE) [13, 14, 15],

$$\dot{\bar{\mathbf{u}}}(t) = \mathbf{r}^{(1)}(\bar{\mathbf{u}}, t) + \int_0^t \tilde{\kappa}(t, s, \bar{\mathbf{u}}) ds \quad (27)$$

354 where the first and second terms are referred to as the Markovian and non-Markovian terms,
355 respectively. The non-Markovian term accounts for the effects of past un-resolved states on
356 the current resolved states via a memory kernel $\tilde{\kappa}(t, s, \bar{\mathbf{u}})$, which in practice is computa-
357 tionally expensive to evaluate.

³⁵⁸ **3.2.1 Markovian Reformulation**

³⁵⁹ This section details the formal derivation of the PIROM as a system of ODEs for the thermal
³⁶⁰ dynamics, based on approximations to the memory kernel. Specifically, the kernel $\tilde{\kappa}$ is
³⁶¹ examined via a leading-order expansion, based on prior work [20]; this can be viewed as an
³⁶² analog of zeroth-order holding in linear system theory with a sufficiently small time step. In
³⁶³ this case, the memory kernel is approximated as,

$$\tilde{\kappa}(t, s, \bar{\mathbf{u}}) \approx \mathbf{r}^{(1)}(\bar{\mathbf{u}}, t) \cdot \nabla_{\bar{\mathbf{u}}} \mathbf{r}^{(2)}(\Phi \bar{\mathbf{u}}, t) \quad (28)$$

³⁶⁴ Note that the terms in $\mathbf{r}^{(1)}$ have a common factor $\bar{\mathbf{A}}^{-1}$; this motivates the following heuristic
³⁶⁵ modification of the model form in eq. (27),

$$\dot{\bar{\mathbf{u}}} = \mathbf{r}^{(1)}(\bar{\mathbf{u}}, t) + \bar{\mathbf{A}}(\mathbf{w})^{-1} \int_0^t \kappa(t, s, \bar{\mathbf{u}}) ds \quad (29a)$$

$$\bar{\mathbf{A}}(\mathbf{w}) \dot{\bar{\mathbf{u}}} = \bar{\mathbf{B}}(\mathbf{w}) \bar{\mathbf{u}} + \bar{\mathbf{f}}(t) + \int_0^t \kappa(t, s, \bar{\mathbf{u}}) ds \quad (29b)$$

³⁶⁶ where the original kernel $\tilde{\kappa}$ is effectively normalized by $\bar{\mathbf{A}}(\mathbf{w})^{-1}$. Intuitively, such choice
³⁶⁷ of kernel reduces its dependency on the averaged material properties, and simplifies the
³⁶⁸ subsequent design of model form.

³⁶⁹ Subsequently, the hidden states are introduced to “Markovianize” the system eq. (27).
³⁷⁰ In this manner, eq. (29b) is converted into a pure state-space model, with the functional
³⁷¹ form of the LCM retained; since LCM is a physics-based model, then it encodes the phys-
³⁷² ical information and retains explicit parametric dependence of the problem. Consider the
³⁷³ representation of the kernel as a finite sum of simpler functions, e.g., exponentials,

$$\kappa(t, s, \bar{\mathbf{u}}) = \sum_{j=1}^m \mathcal{K}_j(t, s, \bar{\mathbf{u}}) [\mathbf{p}_j + \mathbf{d}_j(\bar{\mathbf{u}})] \phi_j(s, \bar{\mathbf{u}}) \quad (30)$$

³⁷⁴ where,

$$\mathcal{K}_j(t, s, \bar{\mathbf{u}}) = e^{-\int_s^t (\lambda_j + e_j(\bar{\mathbf{u}})) d\tau}, \quad \phi_j(s, \bar{\mathbf{u}}) = \mathbf{q}_j^\top \bar{\mathbf{u}}(s) + \mathbf{g}_j(\bar{\mathbf{u}})^\top \bar{\mathbf{u}}(s) + \mathbf{r}_j^\top \bar{\mathbf{f}}(s) \quad (31)$$

³⁷⁵ with suitable coefficients $\mathbf{p}_j, \mathbf{d}_j, \mathbf{q}_j, \mathbf{g}_j, \mathbf{r}_j \in \mathbb{R}^N$ and decay rates $\lambda_j, e_j(\bar{\mathbf{u}}) > 0$, that need to
³⁷⁶ be identified from data.

³⁷⁷ Define the hidden states as,

$$\beta_j(t) = \int_0^t \mathcal{K}_j(s, \bar{\mathbf{u}}) \phi_j(s, \bar{\mathbf{u}}) ds \quad (32)$$

³⁷⁸ and differentiate with respect to time,,

$$\dot{\beta}_j(t) = -[\lambda_j + e_j(\bar{\mathbf{u}})] \beta_j(t) + \mathbf{q}_j^\top \bar{\mathbf{u}}(t) + \mathbf{g}_j(\bar{\mathbf{u}})^\top \bar{\mathbf{u}}(t) + \mathbf{r}_j^\top \bar{\mathbf{f}}(t) \quad (33)$$

³⁷⁹ to obtain the memory,

$$\int_0^t \boldsymbol{\kappa}(t, s, \bar{\mathbf{u}}) ds = \sum_{j=1}^m [\mathbf{p}_j + \mathbf{d}_j(\bar{\mathbf{u}})] \beta_j(t) \quad (34)$$

³⁸⁰ Then, eq. (29b) is recast as the extended Markovian system,

$$\bar{\mathbf{A}}(\mathbf{w}) \dot{\bar{\mathbf{u}}} = \bar{\mathbf{B}}(\mathbf{w}) \bar{\mathbf{u}} + [\mathbf{P} + \mathbf{D}(\bar{\mathbf{u}})] \boldsymbol{\beta} + \bar{\mathbf{f}}(t) \quad (35a)$$

$$\dot{\boldsymbol{\beta}} = [\mathbf{Q} + \mathbf{G}(\bar{\mathbf{u}})] \bar{\mathbf{u}} + [\mathbf{E}(\bar{\mathbf{u}}) - \boldsymbol{\Lambda}] \boldsymbol{\beta} + \mathbf{R} \bar{\mathbf{f}}(t) \quad (35b)$$

³⁸¹ where the data-driven operators associated to the hidden dynamics are collected as,

$$\boldsymbol{\Lambda} = \text{diag}[\lambda_1, \lambda_2, \dots, \lambda_m] \in \mathbb{R}^{m \times m}, \quad \mathbf{P} = [\mathbf{p}_1, \mathbf{p}_2, \dots, \mathbf{p}_m] \in \mathbb{R}^{N \times m} \quad (36a)$$

$$\mathbf{D}(\bar{\mathbf{u}}) = [\mathbf{d}_1(\bar{\mathbf{u}}), \mathbf{d}_2(\bar{\mathbf{u}}), \dots, \mathbf{d}_m(\bar{\mathbf{u}})] \in \mathbb{R}^{N \times m}, \quad \mathbf{Q} = [\mathbf{q}_1, \mathbf{q}_2, \dots, \mathbf{q}_m] \in \mathbb{R}^{m \times N} \quad (36b)$$

$$\mathbf{G}(\bar{\mathbf{u}}) = [\mathbf{g}_1(\bar{\mathbf{u}}), \mathbf{g}_2(\bar{\mathbf{u}}), \dots, \mathbf{g}_m(\bar{\mathbf{u}})] \in \mathbb{R}^{m \times N}, \quad \mathbf{R} = [\mathbf{r}_1, \mathbf{r}_2, \dots, \mathbf{r}_m] \in \mathbb{R}^{m \times N} \quad (36c)$$

$$\mathbf{E}(\bar{\mathbf{u}}) = \text{diag}[e_1(\bar{\mathbf{u}}), e_2(\bar{\mathbf{u}}), \dots, e_m(\bar{\mathbf{u}})] \in \mathbb{R}^{m \times m} \quad (36d)$$

³⁸² The form of the temperature-dependent matrices $\mathbf{D}(\bar{\mathbf{u}})$, $\mathbf{G}(\bar{\mathbf{u}})$, and $\mathbf{E}(\bar{\mathbf{u}})$ is specified in the
³⁸³ next section. Since the hidden states $\boldsymbol{\beta}$ serve as the memory, their initial conditions are set
³⁸⁴ to zero, i.e., $\boldsymbol{\beta}(t_0) = \mathbf{0}$, no memory at the beginning. The physics-infused model in eq. (35)
³⁸⁵ retains the structure of the LCM and depend on the displacements \mathbf{w} , while the hidden states
³⁸⁶ account for missing physics through corrections to the stiffness and advection matrices, as
³⁸⁷ well as the forcing term.

³⁸⁸ 3.2.2 Coupled Physics-Infused Model

³⁸⁹ The next step involves coupling the physics-infused model in eq. (35) with the SRM in
³⁹⁰ eq. (10) to define the PIROM for ablating TPS. To this end, define the surface temperature
³⁹¹ $\mathbf{z}_u \in \mathbb{R}^{\tilde{N}}$ and displacements $\mathbf{z}_w \in \mathbb{R}^{\tilde{N}}$ for $\tilde{N} \leq N$ ablating components so that the observable
³⁹² is given by $\mathbf{z} = [\mathbf{z}_u, \mathbf{z}_w]^\top \in \mathbb{R}^{n_z}$ with $n_z = 2\tilde{N}$ as the total number of observables.

³⁹³ Collect the RPM and hidden states into a single state vector $\mathbf{y} = [\bar{\mathbf{u}}, \mathbf{w}, \boldsymbol{\beta}]^\top \in \mathbb{R}^{n_y}$, where
³⁹⁴ $n_y = N + \tilde{N} + m$, and define a data-driven operator $\mathbf{M} \in \mathbb{R}^{n_z \times n_y}$ to define the PIROM's
³⁹⁵ observable as,

$$\mathbf{z} = \mathbf{M}\mathbf{y} \quad (37)$$

³⁹⁶ where,

$$\mathbf{M} = \begin{bmatrix} \mathbf{M}_{\bar{u}} & \mathbf{0} & \mathbf{M}_{\boldsymbol{\beta}} \\ \mathbf{0} & \mathbf{I} & \mathbf{0} \end{bmatrix} \quad (38)$$

³⁹⁷ includes the matrices $\mathbf{M}_{\bar{u}} \in \mathbb{R}^{\tilde{N} \times N}$ and $\mathbf{M}_{\boldsymbol{\beta}} \in \mathbb{R}^{\tilde{N} \times m}$, which computes the surface tempera-
³⁹⁸ ture observable from the RPM states and hidden states, respectively. The PIROM is coupled
³⁹⁹ to the SRM in eq. (10) by leveraging eq. (37) to compute the surface recession velocity. Thus,

400 the PIROM is formally stated as,

$$\mathcal{A}\dot{\mathbf{y}} = [\mathcal{B} + \mathcal{C}] \mathbf{y} + \mathcal{F}(t) \quad (39a)$$

$$\mathbf{z} = \mathbf{M}\mathbf{y} \quad (39b)$$

401 where,

$$\mathcal{A} = \begin{bmatrix} \bar{\mathbf{A}}(\mathbf{w}) & \mathbf{O} & \mathbf{O} \\ \mathbf{O} & \mathbf{I} & \mathbf{O} \\ \mathbf{O} & \mathbf{O} & \mathbf{I} \end{bmatrix} \in \mathbb{R}^{n_y \times n_y}, \quad \mathcal{B} = \begin{bmatrix} \bar{\mathbf{B}}(\mathbf{w}) & \mathbf{O} & \mathbf{P} \\ \Xi\mathbf{M}_u & \mathbf{O} & \Xi\mathbf{M}_\beta \\ \mathbf{Q} & \mathbf{O} & -\Lambda \end{bmatrix} \in \mathbb{R}^{n_y \times n_y}, \quad (40a)$$

$$\mathcal{C} = \begin{bmatrix} \mathbf{O} & \mathbf{O} & \mathbf{D}(\bar{\mathbf{u}}) \\ \mathbf{O} & \mathbf{O} & \mathbf{O} \\ \mathbf{G}(\bar{\mathbf{u}}) & \mathbf{O} & \mathbf{E}(\bar{\mathbf{u}}) \end{bmatrix} \in \mathbb{R}^{n_y \times n_y}, \quad \mathcal{F} = \begin{bmatrix} \bar{\mathbf{f}}(t) \\ -\tilde{\mathbf{f}} \\ \mathbf{R}\bar{\mathbf{f}}(t) \end{bmatrix} \in \mathbb{R}^{n_y} \quad (40b)$$

402 The learnable parameters in the PIROM are collected as,

$$\Theta = \{\mathbf{P}, \Lambda, \mathbf{Q}, \mathbf{M}, \mathbf{D}(\bar{\mathbf{u}}), \mathbf{G}(\bar{\mathbf{u}}), \mathbf{E}(\bar{\mathbf{u}}), \mathbf{R}\}, \in \mathbb{R}^{n_\theta} \quad (41)$$

403 The matrices $\mathbf{P}, \Lambda, \mathbf{Q}, \mathbf{M}, \mathbf{R}$ are constants, and account for the effects of coarse-graining on
404 the stiffness, output, and forcing matrices. The matrices $\mathbf{D}(\bar{\mathbf{u}}), \mathbf{E}(\bar{\mathbf{u}}), \mathbf{G}(\bar{\mathbf{u}})$ are temperature-
405 dependent matrices, and account for the effects of coarse-graining on the advection matrix
406 due to mesh motion. Leveraging the DG-FEM formula for the advection matrix in eq. (56c)
407 in the Appendix, and noting that the ablating velocity in eq. (4) imposes the boundary
408 condition for the mesh motion, the state-dependent matrices for the i -th component are
409 written as,

$$\mathbf{D}(\bar{\mathbf{u}}) \approx \text{diag}[\dot{\mathbf{w}}] \mathbf{D}, \quad \mathbf{G}(\bar{\mathbf{u}}) \approx \mathbf{G} \text{diag}[\dot{\mathbf{w}}], \quad \mathbf{E}(\bar{\mathbf{u}}) \approx \text{diag} \left[\underbrace{\dot{\mathbf{w}}, \dots, \dot{\mathbf{w}}}_{\tilde{m} \text{ times}} \right] \mathbf{E} \quad (42)$$

410 where $\dot{\mathbf{w}} = \dot{\mathbf{w}}(\bar{\mathbf{u}})$ is the SRM based on the observable temperature $\bar{\mathbf{u}}$ and \tilde{m} is the number
411 of hidden states per component so that $m = N\tilde{m}$.

412 The PIROM in eq. (39) incorporates explicit information on the material properties,
413 boundary conditions, and surface recession, and is designed to generalize across parametric
414 variations in these inputs. Moreover, the hidden dynamics in eq. (35) are interpretable, as
415 these retain the functional form of the DG-FEM in eq. (7). The next step is focused on
416 identifying the unknown data-driven parameters Θ characterizing the hidden dynamics.

417 3.3 Learning the Hidden Dynamics

418 Learning of the PIROM is achieved through a gradient-based neural-ODE-like approach [3].
419 For ease of presentation, consider the compact form of the PIROM in eq. (39),

$$\mathcal{D}(\dot{\mathbf{y}}, \mathbf{y}, \xi, \mathcal{F}; \Theta) = \mathbf{0} \quad (43)$$

420 where $\boldsymbol{\xi}$ defines the model parameters, i.e., SRM parameters, while \mathcal{F} represents the forcing
 421 terms, i.e., the boundary conditions.

422 Consider a dataset of N_s high-fidelity *surface temperature* observable trajectories \mathbf{z}_{HF} ,
 423 sampled at p time instances $\{t_k\}_{k=0}^{p-1}$, for different parameter settings $\{\boldsymbol{\xi}^{(l)}\}_{l=1}^{N_s}$ and forcing
 424 functions $\{\mathcal{F}^{(l)}(t)\}_{l=1}^{N_s}$. The dataset is expressed as,

$$\mathcal{D} = \left\{ \left(t_k, \mathbf{z}_{\text{HF}}^{(l)}(t_k), \boldsymbol{\xi}^{(l)}, \mathcal{F}^{(l)}(t_k) \right) \right\}_{l=1}^{N_s}, \quad k = 0, 1, \dots, p-1 \quad (44)$$

425 In this work, the dataset contains only surface temperature observables – all high-fidelity
 426 information regarding the surface displacements *are assumed to be unavailable during learning*.
 427

428 The learning problem is formulated as the following differentially-constrained problem,

$$\min_{\Theta} \mathcal{J}(\Theta; \mathcal{D}) = \sum_{l=1}^{N_s} \int_{t_0}^{t_f} \ell \left(\mathbf{z}_u^{(l)}, \mathbf{z}_{\text{HF}}^{(l)} \right) dt \quad (45a)$$

$$\text{s.t. } \mathbf{0} = \mathcal{D} \left(\dot{\mathbf{y}}^{(l)}, \mathbf{y}^{(l)}, \boldsymbol{\xi}^{(l)}, \mathcal{F}^{(l)}; \Theta \right) \quad (45b)$$

429 for $l = 1, 2, \dots, N_s$, the objective is to minimize the discrepancy between the high-fidelity
 430 and PIROM predictions for the l -th trajectory with $\ell \left(\mathbf{z}_u^{(l)}, \mathbf{z}_{\text{HF}}^{(l)} \right) = \left\| \mathbf{z}_u^{(l)} - \mathbf{z}_{\text{HF}}^{(l)} \right\|_2^2$.

431 The gradient-based optimization loop is based on the adjoint variable $\boldsymbol{\lambda}$, governed by the
 432 adjoint differential equation,

$$\frac{\partial \ell}{\partial \mathbf{y}} + \boldsymbol{\lambda}^\top \frac{\partial \mathcal{D}}{\partial \mathbf{y}} - \frac{d}{dt} \left(\boldsymbol{\lambda}^\top \frac{\partial \mathcal{D}}{\partial \dot{\mathbf{y}}} \right) = \mathbf{0} \quad (46a)$$

$$\boldsymbol{\lambda}(t_f)^\top \frac{\partial \mathcal{D}}{\partial \dot{\mathbf{y}}(t_f)} = \mathbf{0} \quad (46b)$$

433 Once $\boldsymbol{\lambda}$ is solved, the gradient is computed as,

$$\nabla_\Theta \mathcal{J} = \frac{1}{N_s} \sum_{l=1}^{N_s} \int_{t_0}^{t_f} \left(\frac{\partial \ell}{\partial \Theta} + \left(\boldsymbol{\lambda}^{(l)} \right)^\top \frac{\partial \mathcal{D}}{\partial \Theta} \right) dt \quad (47)$$

434 The PIROM parameters Θ are updated via stochastic gradient descent using ML optimizers
 435 such as Adam. The learning procedure iterates between solving the PIROM in eq. (43)
 436 forward in time, solving the adjoint equation in eq. (46) backward in time, and updating the
 437 parameters Θ until convergence.

4 Application to Thermal Protection Systems

438 In this section, the proposed PIROM approach is applied to the analysis of thermo-ablative
 439 multi-layered hypersonic TPS. The performance of the PIROM is evaluated in terms of the
 440 three corners of the ITM in Fig. 1, based on parametric variations of boundary conditions and
 441 SRMs. The results show PIROM to be a promising candidate for the solution of the impos-

Component	w (cm)	h (cm)	ρ (kg/m ³)	c_p (J/kg·K)	k (W/m·K)	$\alpha \times 10^{-6}$ (m/s·K)
#1	0.3	0.03	160	1200	0.2	1
#2	0.3	0.03	1800	900	5	1
#3	0.3	0.03	300	1500	0.15	1
#4	0.9	0.03	1600	800	10	0

Table 1: Description of TPS components, including thickness h , density ρ , specific heat capacity c_p , thermal conductivity k , and SRM parameter α .

443 sible trinity of modeling, achieving RPM-level computational efficiency and generalizability,
 444 while attaining high-fidelity model accuracy.

445 4.1 Problem Definition

446 Consider the two-dimensional TPS configuration shown in Fig. 3 with constant material
 447 properties within each layer, dimensions, and BCs listed in Table 1. Such configuration is
 448 representative of the TPS used for the initial concept 3.X vehicle in past studies [10], and in-
 449 volves two main layers: an outer ablative layer, and an inner substrate layer. The top ablative
 450 layer may be composed of different materials, such as PICA or Avcoat, while the substrate
 451 layer is typically made of a high-temperature resistant material, such as carbon-carbon com-
 452 posite [7]. The ablative layer, composed of $\tilde{N} = 3$ ablative components, is subjected to
 453 strong time-varying and non-uniform heating, while the substrate layer, composed of one
 454 non-ablative component, is insulated adiabatically at the outer surface; the total number of
 455 components is thus $N = 4$.

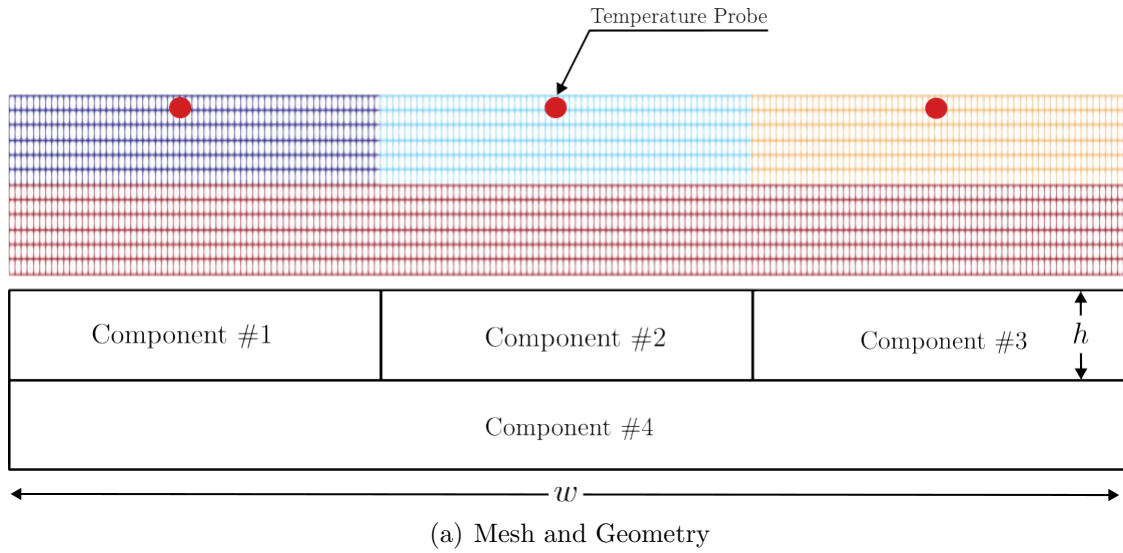
456 The lumped-mass representation of the TPS configuration is shown in Fig. 3(b), where
 457 each component Ω_i is represented by a lumped mass with uniform temperature $u_i(t)$. Details
 458 regarding the derivation of the LCM for this configuration are provided in Appendix A.
 459 The sources of non-linearities studied in this problem originate from the coupling between
 460 the thermodynamics and temperature-dependent mesh motion, i.e., geometry-dependent
 461 matrices, as well as the heterogeneities across material layers. As shown in Fig. 3, perfect
 462 thermocouple devices are placed at the surfaces of the ablative layers for the collection of
 463 the high-fidelity temperature signals that are used in the following sections for training and
 464 testing the PIROM.

465 4.2 Problem Parametrization

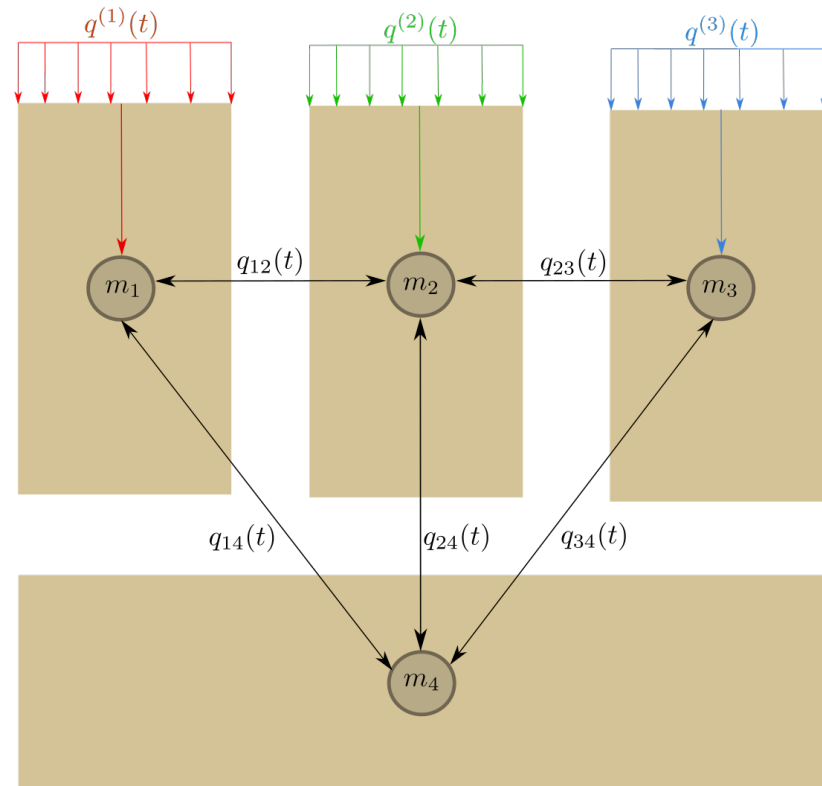
466 The operating conditions of the TPS are specified by the boundary conditions, i.e., the heat
 467 flux, and the SRM matrix $\boldsymbol{\Xi}$. Specifically, the heat flux on the Neumann BC is parametrized
 468 using $\boldsymbol{\xi}_{\text{BC}} = \{\xi_1, \xi_2, \xi_3\}$, while the SRM is parametrized using $\boldsymbol{\xi}_{\text{SRM}} = \{\alpha_1, \alpha_2, \alpha_3\}$. Thus,
 469 the heat flux and SRM over the i -th ablative component are expressed as,

$$q_i(x, t; \boldsymbol{\xi}_{\text{BC}}) = \xi_1 e^{\xi_2 x} e^{\xi_3 t}, \quad \forall x \in \Gamma_{i,q}, \quad \dot{w}_i(z_{u,i}; \boldsymbol{\xi}_{\text{SRM}}) = \alpha_i (z_{u,i} - u_{0,i}), \quad i = 1, \dots, \tilde{N} \quad (48)$$

470 where $\Gamma_{i,q}$, $z_{u,i}$, and $u_{0,i}$ correspond to the Neumann BC surface, the surface temperature
 471 prediction, and the initial temperature of the i -th ablative component, respectively. The



(a) Mesh and Geometry



(b) Lumped Mass Representation

Figure 3: Four-component TPS geometry and lumped-mass representation for the TPS.

Dataset	Parameters					
	$\xi_1 \times 10^3$	$\xi_2 \times 10^{-1}$	$\xi_3 \times 10^{-2}$	$\alpha_1 \times 10^{-6}$	$\alpha_2 \times 10^{-6}$	$\alpha_3 \times 10^{-6}$
\mathcal{D}_1	[-6.059, -5.902]	[-3.501, 3.152]	[9.670, 10.464]	1	1	1
\mathcal{D}_2	[-6.122, -5.887]	[-3.601, -3.074]	[9.218, 11.246]	1	1	1
\mathcal{D}_3	6	-3.333	10	[0.6, 1.5]	[0.6, 1.5]	[0.6, 1.5]

Table 2: Range of parameters [min, max] in training and testing datasets.

parameters ξ_1 , ξ_2 , and ξ_3 control the heat flux magnitude, spatial variation, and temporal variation, respectively. The constant α_i is a small material-dependent constant determined from the B' table [12], specifying the surface recession velocity for a given temperature.

4.3 Data Generation

Full-order solutions of the TPS are computed using the FEM multi-mechanics module from the **Aria** package with the mesh shown in Fig. 3(a) [4]. The mesh consists of 2196 total elements, with 366 elements for each ablative component and 1098 elements for the substrate component. Given an operating condition $\boldsymbol{\xi} = [\boldsymbol{\xi}_{\text{BC}}, \boldsymbol{\xi}_{\text{SRM}}]^{\top}$, a high-fidelity solution is computed for one minute, starting from an uniform initial temperature of $T(x, t_0) = 300$ K. Each solution consist of a collection of space-time-varying temperature and displacement fields $\left\{ \left(t_k, \mathbf{u}_{\text{HF}}^{(l)}(t_k), \mathbf{d}_{\text{HF}}^{(l)}(t_k), \boldsymbol{\xi}^{(l)} \right) \right\}_{k=0}^{p-1}$, where p is the number of time steps with a step size of $\Delta t \approx 10^{-3}$. The observable trajectories are representative of near-wall thermocouple sensing of hypersonic flows involving heat transfer. At each time instance t_k , a temperature reading is recorded from each ablative component using the thermocouples shown in Fig. 3, resulting in three temperature signals, i.e., the observables $\mathbf{z}_{\text{HF}} \in \mathbb{R}^3$. Therefore, each full-order solution produces one trajectory of observables $\left\{ \left(t_k, \mathbf{z}_{\text{HF}}^{(l)}(t_k), \boldsymbol{\xi}^{(l)} \right) \right\}_{k=0}^{p-1}$. The goal of the PIROM is to predict the surface temperature and displacement as accurately as possible.

4.3.1 Definition of Training and Testing Datasets

The range of parameters used to generate the training \mathcal{D}_1 and testing $\{\mathcal{D}_2, \mathcal{D}_3\}$ datasets are listed in Table 2. The training and testing datasets are designed, respectively, to: (1) minimize the information that the PIROM can “see”, and (2) to maximize the variability of test operating conditions to examine the PIROM’s generalization performance. A total of 110 normally-distributed data points for the BC parametrization are visualized in Fig. 4(a), and the corresponding observable trajectories are shown in Figs. 4(b) and 4(c). The training dataset \mathcal{D}_1 includes 10 trajectories with randomly selected BC parameters from the 110 points, with nominal SRM parameters $\boldsymbol{\xi}_{\text{SRM}} = \{1, 1, 1\} \times 10^{-6}$. Note that although Fig. 4(c) shows the surface displacements for all ablative components in \mathcal{D}_1 , only the *surface temperature is used for training the PIROM*.

Two additional datasets are generated for testing. The dataset \mathcal{D}_2 includes the remaining 100 BC parameter values not considered in \mathcal{D}_1 , and the high-fidelity simulation are generated with the same nominal SRM parameters. The cases in the \mathcal{D}_3 fixes the boundary condition as shown in Fig. 4(a) and varies the SRM parameters as shown in Table. 2. The testing

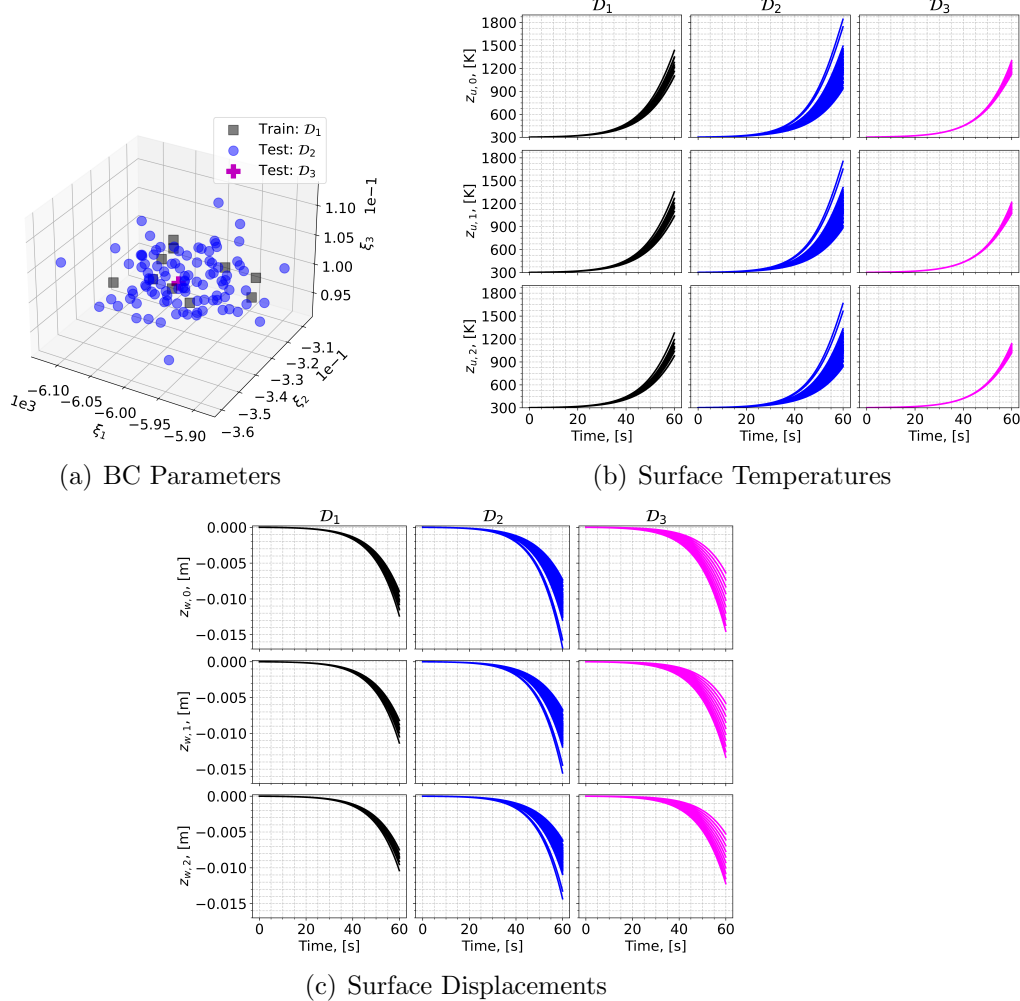


Figure 4: Boundary condition parameters, temperature observables, and displacement observables for the training and testing datasets. The variables $z_{u,i}$ and $z_{w,i}$ correspond to the surface temperature and displacement of the i -th ablative component, respectively.

504 datasets D_2 and D_3 are *out-of-distribution* (OOD) datasets, and are meant for testing the
 505 generalizability of the ROMs to unseen BCs and SRMs, respectively.

506 4.4 Performance Metrics

507 The performance of the PIROM is evaluated by the metrics of prediction error and computa-
 508 tional cost.

509 **Prediction Error** Consider one trajectory of high-fidelity surface temperature and dis-
 510 placement data $\left\{ \left(t_k, \mathbf{z}_{u,\text{HF}}^{(l)}(t_k), \mathbf{z}_{w,\text{HF}}^{(l)}(t_k) \right) \right\}_{k=0}^{p-1}$ for the l -th operating condition in the testing
 511 datasets D_2 or D_3 . The difference $e_i^{(l)}$ for the i -th predicted observable, denoted as $z_i^{(l)}$, is

512 computed as,

$$e_i^{(l)} = \frac{1}{\Delta z_i^{(l)}} \sqrt{\frac{1}{p} \sum_{k=0}^{p-1} \left(z_{i,\text{HF}}^{(l)}(t_k) - z_i^{(l)}(t_k) \right)^2} \quad (49)$$

513 for $i = 1, 2, 3$ and $z_i^{(l)} \in \{z_{i,u}^{(l)}, z_{i,w}^{(l)}\}$, and where,

$$\Delta z_i^{(l)} = \max_{0 \leq k \leq p-1} z_{i,\text{HF}}^{(l)}(t_k) - \min_{0 \leq k \leq p-1} z_{i,\text{HF}}^{(l)}(t_k) \quad (50)$$

514 Subsequently, the prediction error of one trajectory is computed by a weighted sum based
 515 on the area of each *ablative component*, resulting in the normalized root mean square error
 516 (NRMSE) metric for one trajectory,

$$\text{NRMSE} = \frac{\sum_{i=1}^{\tilde{N}} |\Omega_i| e_i^{(l)}}{\sum_{i=1}^{\tilde{N}} |\Omega_i|} \times 100\% \quad (51)$$

517 For one dataset, the NRMSE is defined to be the average of the NRMSEs of all trajectories
 518 in the dataset.

519 **Computational Acceleration** The *computational acceleration* metric focuses on the quan-
 520 tification of the speedup factor $\frac{\mathcal{T}_{\text{HF}}(\mathcal{D})}{\mathcal{T}_{\mathcal{M}}(\mathcal{D})}$, where $\mathcal{T}_{\text{HF}}(\mathcal{D})$ and $\mathcal{T}_{\mathcal{M}}(\mathcal{D})$ correspond to the wall-clock
 521 time required by the high-fidelity model and the reduced-order model \mathcal{M} (i.e., PIROM or
 522 RPM) to evaluate all trajectories in the dataset \mathcal{D} , respectively. For a benchmark analysis
 523 of the computational costs during the training phase, please refer to Ref. [18].

524 4.5 Generalization to Boundary Conditions

525 To assess generalization to BC, the PIROM and RPM are evaluated on the \mathcal{D}_2 dataset. Tem-
 526 perature trajectory predictions for a representative test case are shown in Figs. 5(a) and 5(b),
 527 where the PIROM accurately captures the surface temperature and displacement dynamics,
 528 while the RPM exhibits larger deviations and under-predicts surface displacements due to
 529 the averaging effects of the LCM. The mean NRMSE across all test cases in \mathcal{D}_2 is shown
 530 in Figs. 5(e) and 5(f), where the PIROM consistently achieves errors of $\approx 0.5\%$ for both
 531 temperature and displacement predictions, improving the RPM's accuracy by an order of
 532 magnitude. Figure 5 reports the average substrate temperature, where the LCM remains
 533 highly accurate due to the symmetric TPS geometry, adiabatic BCs, and negligible thermal
 534 gradients within the substrate. Although the PIROM is trained only on the surface tem-
 535 peratures of the three ablative components, its hidden dynamics retain the LCM's accuracy
 536 for this untrained observable, demonstrating the PIROM's ability to generalize and preserve
 537 the underlying physics of the reduced-physics backbone.

538 **4.6 Generalization to Surface Recession Models**

539 The generalization performance of the PIROM and RPM is also evaluated on surface recess-
540 sion models using the \mathcal{D}_3 dataset. As detailed in Table 1, the SRM parameter α in \mathcal{D}_3 is
541 perturbed 10 times by up to $\pm 50\%$ from their nominal values. The SRM model perturbation
542 introduces significant changes to the ablative layer dynamics, potentially increasing the rate
543 of ablation at lower temperatures, as shown in Figs. 5(c) and 5(d). The PIROM, without
544 considering any SRM variations during training, is able to accurately predict the surface tem-
545 perature and displacement dynamics for the perturbed SRMs. Figures 5(e) and 5(f) show
546 the mean NRMSE across all test cases in \mathcal{D}_3 , where the PIROM consistently achieves errors
547 below 1.5% for both temperature and displacement predictions, and consistently improves
548 the RPM’s accuracy by approximately an order of magnitude.

549 **4.7 Computational Cost**

550 All computations are performed in serial for fairness on an Intel Xeon (R) Gold 6258R
551 CPU 2.70GHz computer with 62 GB of RAM. The numerical integration for the RPM
552 and PIROM models are performed using SciPy’s `solve_ivp` function with default settings.
553 Provided a parametrization for the BC and SRM, the high-fidelity FEM simulation takes
554 about ≈ 60 seconds, the RPM takes about ≈ 0.137 seconds, and the PIROM takes about
555 ≈ 0.280 seconds. Therefore, during evaluation both the RPM and PIROM achieve speedup
556 factors of approximately 438 and 214, respectively, over the high-fidelity model. As a result,
557 the PIROM and RPM are *two-orders-of-magnitude faster* than the high-fidelity model. The
558 PIROM nearly preserves the computational efficiency of the RPM (about twice as expensive
559 as the RPM), while achieving significantly higher accuracy and generalization capabilities.
560 The results demonstrate the benefits of physics-infused modeling for the development of
561 efficient and generalizable ROMs for complex multi-physics systems.

562 **4.8 Summary of Results**

563 The results presented in this section demonstrate the accuracy, generalizability, and com-
564 putational efficiency of the proposed PIROM approach for the analysis of thermo-ablative
565 multi-layered hypersonic TPS. The PIROM consistently achieves low prediction errors below
566 1% for both surface temperature and displacement across a range of unseen boundary con-
567 ditions and surface recession models. Furthermore, the PIROM retains the computational
568 efficiency of traditional RPMs, achieving speedup factors of over 200 times compared to high-
569 fidelity FEM simulations. The generalization capabilities of the PIROM are attributed to its
570 hybrid structure: a physics-based LCM backbone that ensures consistency with the under-
571 lying thermodynamics, while a data-driven correction mechanism captures the un-resolved
572 dynamics.

573 **5 Conclusions**

574 This work presents the development and validation of the *scientific machine learning* frame-
575 work termed *Physics-Informed Reduced Order Model* (PIROM) for simulating the transient

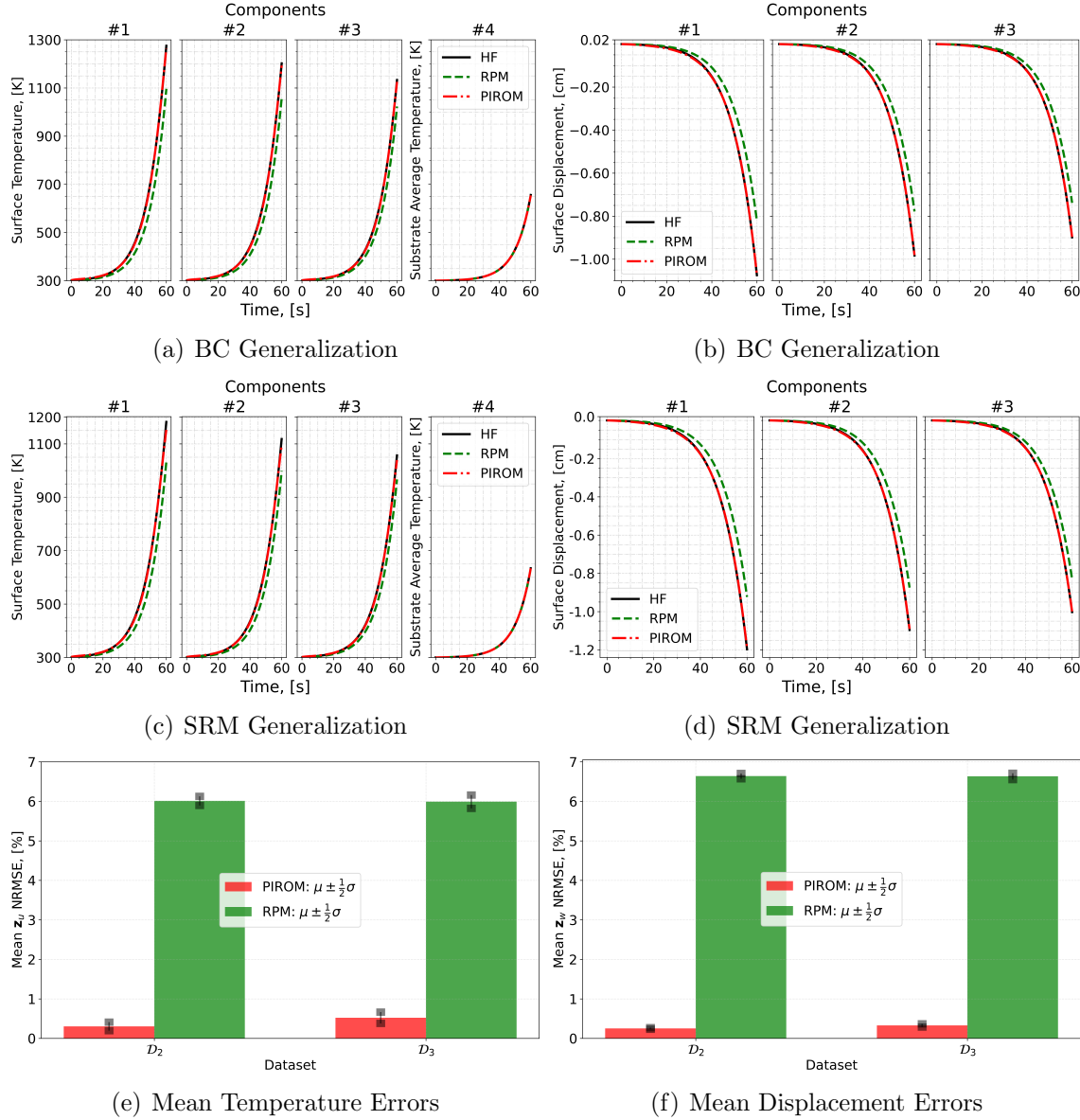


Figure 5: PIROM predictions against high-fidelity solutions for (a)-(b) BC generalization, (c)-(d) SRM generalization, and (e)-(f) mean errors across testing datasets.

576 thermo-ablative response of hypersonic thermal protection systems (TPS) subjected to hy-
577 personic aerodynamic heating. Using coarse-graining on a DG-FEM model and the Mori-
578 Zwanzig formalism, the PIROM formulation in Ref. [18] is extended to account for non-
579 decomposing ablative material response. The PIROM builds upon the following two key
580 components: (1) a first-order physics-based model, i.e., the LCM and SRM, for low-fidelity
581 predictions of the transient thermo-ablative TPS response; and (2) a data-driven closure to
582 the non-Markovian term in the generalized Langevin equation (GLE). The non-Markovian
583 closure is recast as a set of hidden states that evolve according to a data-driven dynamical
584 system that is learned from a sparse collection of high-fidelity temperature signals.

585 The results demonstrate that the PIROM framework effectively reconciles the trade-
586 offs between accuracy, generalizability, and efficiency of the ITM for simulating ablating
587 hypersonic TPS. The PIROM consistently achieves mean observable prediction errors of
588 $\approx 0.5\%$ for a wide range of extrapolative settings of model parameters, involving time-and-
589 space varying boundary conditions and SRM models. Notably, the PIROM improves the
590 RPM's accuracy by an order of magnitude while preserving its computational efficiency,
591 physical interpretability, and parametric generalizability. Moreover, the PIROM delivers
592 online evaluations that are two orders of magnitude faster than the FOM. These results
593 highlight the PIROM's potential as a promising framework for optimizing multi-physical
594 dynamical systems, such as TPS under diverse operating conditions.

595 A Technical Details

596 This appendix presents the technical details of the PIROM framework applied to the trans-
 597ient modeling of thermo-ablative TPS. The first section provides the mathematical details
 598 for the definition of the DG-FEM. The second section details the coarse-graining proce-
 599 dures performed on the DG-FEM representation of the TPS. The third section presents the
 600 derivation of the LCM model from an energy-conservation perspective.

601 A.1 Full-Order Model

602 To obtain the full-order numerical solution, the governing equation is spatially discretized
 603 using variational principles of Discontinuous Galerkin (DG) to result in a high-dimensional
 604 system of ordinary differential equations (ODEs). The DG-FEM model is written in an
 605 element-wise form, which is beneficial for subsequent derivations of the lower-order models.
 606 Note that the choice of DG approach here is mainly for theoretical convenience in the sub-
 607 sequent coarse-graining formulation. In the numerical results, the full-order TPS ablation
 608 simulations is computed using standard FEM instead, and the equivalence between DG and
 609 standard FEM is noted upon their convergence.

610 A.1.1 Domain Discretization

611 Consider a conforming mesh partition of the domain in Fig. 3, where each element belongs
 612 to one and only one component. Denote the collection of all M elements as $\{E_i\}_{i=1}^M$. To ease
 613 the description of the DG model, a graph structure is employed. The elements are treated
 614 as vertices, the set of which is denoted $\mathcal{V} = \{m\}_{m=1}^M$. Two neighboring elements, E_i and E_j ,
 615 are connected by an edge (i, j) , and the shared boundary between them is denoted e_{ij} . The
 616 collection of all edges are denoted \mathcal{E} , and \mathcal{G} is referred to as a graph. In the graph, the edges
 617 are unidirected, meaning if $(i, j) \in \mathcal{E}$ then $(j, i) \in \mathcal{E}$. Furthermore, denote the neighbors
 618 of the i -th element as $\mathcal{N}_i = \{j | (i, j) \in \mathcal{E}\}$. Lastly, for the ease of notation, introduce two
 619 special indices: T for the boundary of an element that overlaps with the Dirichlet boundary
 620 condition, and similarly q for the Neumann boundary condition.

621 A.1.2 Weak Form of Discontinuous Galerkin Method

622 Choosing appropriate basis functions ϕ_k and ϕ_l and using the Interior Penalty Galerkin
 623 (IPG) scheme [5], the variational bilinear form for eq. (1a) is,

$$\sum_{i=1}^M a_{\epsilon,i}(\phi_k, \phi_l) = \sum_{i=1}^M L_i(\phi_k) \quad (52)$$

624 where ϵ is an user-specified parameter and,

$$a_{\epsilon,i}(\phi_k, \phi_l) = \int_{E_i} \left(\rho c_p \phi_k \frac{\partial \phi_l}{\partial t} + \mathbf{k} \nabla \phi_k \cdot \nabla \phi_l - \rho c_p \phi_k \mathbf{v} \cdot \nabla \phi_l \right) dE_i \quad (53a)$$

$$\begin{aligned} & - \sum_{j \in \mathcal{N}_i \cup \{T_b\}} \int_{e_{ij}} \{ \mathbf{k} \nabla \phi_k \cdot n \} [\phi_l] de_{ij} + \epsilon \sum_{j \in \mathcal{N}_i \cup \{T_b\}} \int_{e_{ij}} \{ \mathbf{k} \nabla \phi_l \cdot n \} [\phi_k] de_{ij} \\ & + \sigma \sum_{j \in \mathcal{N}_i \cup \{T_b\}} \int_{e_{ij}} [\phi_k] [\phi_l] de_{ij} \end{aligned} \quad (53b)$$

$$L_i(v) = \epsilon \sum_{j \in \mathcal{N}_i \cup \{T_b\}} \int_{e_{ij}} (\mathbf{k} \nabla \phi_l \cdot n) T_b de_{ij} + \int_{e_{iq}} \phi_k q_b de_{iq} + \sigma \int_{e_{iT}} \phi_k T_b de_{iT} \quad (53c)$$

625 In the bi-linear form above, the notations $[]$ and $\{ \}$ are respectively the jumps and averages
626 at the boundary e_{ij} share by two elements E_i and E_j ,

$$[u] = u|_{E_i} - u|_{E_j}, \quad \{u\} = \frac{1}{2} \left(u|_{E_i} + u|_{E_j} \right), \quad \text{for } x \in e_{ij} = E_i \cap E_j$$

627 Moreover, the terms associated with σ are introduced to enforce the Dirichlet boundary
628 conditions; σ is a penalty factor whose value can depend on the size of an element. Depending
629 on the choice of ϵ , the bi-linear form corresponds to symmetric IPG ($\epsilon = -1$), non-symmetric
630 IPG ($\epsilon = 1$), and incomplete IPG ($\epsilon = 0$). All these schemes are consistent with the
631 original PDE and have similar convergence rate with respect to mesh size. In the following
632 derivations, the case $\epsilon = 0$ is chosen for the sake of simplicity.

633 A.1.3 Discontinuous Galerkin Model

634 Next, the DG-based model is written in an element-wise form. For the i -th element, use a
635 set of P trial functions to represent the temperature as in eq. (6). Without loss of generality,
636 the trial functions are assumed to be orthogonal, so that,

$$\int_{E_i} \phi_l^i(x) \phi_k^i(x) d\Omega = 0, \quad l \neq k$$

637 where $|E_i|$ is the area ($n_d = 2$) or volume ($n_d = 3$) of the i -th element, and δ_{lk} is the Kronecker
638 delta function. Furthermore, for simplicity, choose $\phi_1^i = 1$. Thus, by orthogonality,

$$\int_{E_i} \phi_1^i(x) d\Omega = |E_i|, \quad \int_{E_i} \phi_k^i(x) d\Omega = 0, \quad k = 2, 3, \dots, P$$

639 Under the choice of basis functions, u_1^i is simply the average temperature of element E_i ,
640 denoted as \bar{u}_i .

641 Using test functions same as trial functions, the dynamics $\mathbf{u}^{(i)}$ is obtained by evaluating
642 the element-wise bi-linear forms,

$$a_{\epsilon,i}(\phi_k^{(i)}, T^{(i)}) = L_i(\phi_k^{(i)}), \quad k = 1, 2, \dots, P \quad (54)$$

643 Therefore, by standard variational principles, e.g., [5], the element-wise governing equation
644 is denoted as,

$$\mathbf{A}_i \dot{\mathbf{u}}_i = (\mathbf{B}_i + \mathbf{C}_i) \mathbf{u}_i + \sum_{j \in \mathcal{N}_i \cup \{T_b\}} (\mathbf{B}_{ij}^i \mathbf{u}_i + \mathbf{B}_{ij}^j \mathbf{u}_j) + \mathbf{f}_i(t), \quad \text{for } i = 1, 2, \dots, M \quad (55)$$

645 where for $k, l = 1, 2, \dots, P$,

$$[\mathbf{A}^{(i)}]_{kl} = \int_{E_i} \rho c_p \phi_k^{(i)} \phi_l^{(i)} dE_i \quad (56a)$$

$$[\mathbf{B}^{(i)}]_{kl} = - \int_{E_i} (\nabla \phi_k^{(i)}) \cdot (\mathbf{k} \nabla \phi_l^{(i)}) dE_i \quad (56b)$$

$$[\mathbf{C}^{(i)}]_{kl} = \int_{E_i} \rho c_p \phi_k^{(i)} \mathbf{v}^{(i)} \cdot \nabla \phi_l^{(i)} dE_i \quad (56c)$$

$$[\mathbf{B}_{ij}^{(i)}] = \int_{e_{ij}} \left\{ \mathbf{k} \nabla \phi_k^{(i)} \cdot \hat{n} \right\} \phi_l^{(i)} - \sigma [\phi_k^{(i)}] \phi_l^{(i)} de_{ij} \quad (56d)$$

$$[\mathbf{B}_{ij}^{(j)}] = \int_{e_{ij}} - \left\{ \mathbf{k} \nabla \phi_k^{(i)} \cdot \hat{n} \right\} \phi_l^{(j)} + \sigma [\phi_k^{(i)}] \phi_l^{(j)} de_{ij} \quad (56e)$$

$$[\mathbf{f}^{(i)}]_k = \int_{e_{iq}} \phi_k^{(i)} q_b de_{iq} + \sigma \int_{e_{iT}} \phi_k^{(i)} de_{iT} \quad (56f)$$

646 The matrices $\mathbf{A}^{(i)} \in \mathbb{R}^{P \times P}$, $\mathbf{B}^{(i)} \in \mathbb{R}^{P \times P}$, and $\mathbf{C}^{(i)} \in \mathbb{R}^{P \times P}$ are respectively the capacitance,
647 conductivity, and advection matrices for element i . These matrices depend on ρ , c_p , \mathbf{k} , and
648 \mathbf{v} , and hence can be non-linear functions of $\mathbf{u}^{(i)}$. Since the trial functions are orthogonal, if
649 ρc_p is constant within an element, $\mathbf{A}^{(i)}$ is diagonal; otherwise, \mathbf{A}_i is symmetric and positive
650 definite as $\rho c_p > 0$.

651 For compactness, the element-wise model in eq. (55) is also written in matrix form,

$$\mathbf{A} \dot{\mathbf{u}} = [\mathbf{B} + \mathbf{C}(\mathbf{u})] \mathbf{u} + \mathbf{f}(t) \quad (57)$$

652 where $\mathbf{u} = [\mathbf{u}^{(1)}, \mathbf{u}^{(2)}, \dots, \mathbf{u}^{(M)}]^T \in \mathbb{R}^{MP}$ includes all DG variables, $\mathbf{f} = [\mathbf{f}^{(1)}, \mathbf{f}^{(2)}, \dots, \mathbf{f}^{(M)}]^T \in$
653 \mathbb{R}^{MP} , \mathbf{A} and \mathbf{C} are matrices of M diagonal blocks whose i -th blocks are $\mathbf{A}^{(i)}$ and $\mathbf{C}^{(i)}$, and
654 \mathbf{B} is a matrix of $M \times M$ blocks whose (i, j) -th block is,

$$\mathbf{B}_{ij} = \begin{cases} \mathbf{B}^{(i)} + \sum_{j \in \mathcal{N}_i \cup \{T_b\}} \mathbf{B}_{ij}^{(i)}, & i = j \\ \mathbf{B}_{ij}^{(j)}, & i \neq j \end{cases} \quad (58)$$

655 The dependency of \mathbf{C} on \mathbf{u} is explicitly noted in eq. (57), which is the main source of non-
656 linearity in the current TPS problem. Moreover, the mesh velocity \mathbf{v} varies with space
657 and time, and thus the advection matrix \mathbf{C} varies with time as a function of the surface
658 temperature $T_q(x, t)$.

659 A.2 Coarse-Graining of Dynamics

660 The LCM is obtained by coarse-graining the full-order DG-FEM. This coarse-graining procedure produces resolved $\mathbf{r}^{(1)}(\mathbf{u}, t)$ and residual $\mathbf{r}^{(2)}(\mathbf{u}, t)$ dynamics as in eq. (24). This section 661 presents the detail derivations and magnitude analysis for the resolved and residual dynamics. 662

664 A.2.1 Resolved Dynamics

665 Using eq. (21), the resolved dynamics is computed as follows,

$$\mathbf{r}^{(1)}(\bar{\mathbf{u}}, t) = \mathcal{P} [\Phi^+ \mathbf{A}^{-1} (\mathbf{B}\mathbf{u} + \mathbf{C}(\mathbf{u})\mathbf{u} + \mathbf{f}(t))] \quad (59a)$$

$$= \Phi^+ \mathbf{A}^{-1} \mathbf{P} \mathbf{B} \mathbf{P} \mathbf{u} + \Phi^+ \mathbf{A}^{-1} \mathbf{P} \mathbf{C} (\mathbf{P} \mathbf{u}) \mathbf{P} \mathbf{u} + \Phi^+ \mathbf{A}^{-1} \mathbf{P} \mathbf{f}(t) \quad (59b)$$

$$= \underbrace{\Phi^+ \mathbf{A}^{-1} \Phi}_{\#1} \underbrace{\Phi^+ \mathbf{B} \Phi \bar{\mathbf{u}}}_{\#2} + \Phi^+ \mathbf{A}^{-1} \Phi \underbrace{\Phi^+ \mathbf{C} (\Phi \bar{\mathbf{u}}) \Phi}_{\#3} \bar{\mathbf{u}} + \Phi^+ \mathbf{A}^{-1} \Phi \underbrace{\Phi^+ \mathbf{f}(t)}_{\#4} \quad (59c)$$

666 Detailed derivations for the #1, #2, and #4 terms can be found in Ref. [18] for the case of 667 temperature-varying matrices. The effects of coarse-graining on the advection term #3 are 668 analyzed next.

669 **Term #3** The $\mathbf{C}(\mathbf{u}) \in \mathbb{R}^{MP \times MP}$ matrix contains M diagonal of size $P \times P$, since the 670 basis functions are defined locally on each element. Therefore, $[\mathbf{C}(\mathbf{u})]_{ij} = \mathbf{0}$ for all $i \neq j$ with 671 $i, j = 1, 2, \dots, M$. It follows that for $k, l = 1, 2, \dots, N$,

$$[\Phi^+ \mathbf{C}(\Phi \bar{\mathbf{u}}) \Phi]_{kl} = \sum_{i=1}^M \sum_{j=1}^M \varphi_i^{k+} [\mathbf{C}(\Phi \bar{\mathbf{u}})]_{ij} \varphi_j^l \quad (60a)$$

$$= \sum_{i=1}^M \varphi_i^{k+} [\mathbf{C}(\Phi \bar{\mathbf{u}})]_{ii} \varphi_i^l \quad (60b)$$

$$= \sum_{i \in \mathcal{V}_k} \varphi_i^{k+} [\mathbf{C}(\Phi \bar{\mathbf{u}})]_{ii} \varphi_i^l \quad (60c)$$

672 where in the second row, the fact that $[\mathbf{C}(\mathbf{u})]_{ij} = 0$ for all $i \neq j$ is used, and in the last row, 673 the fact that $\varphi_i^{k+} = 0$ for all $i \notin \mathcal{V}_k$ is used. Now, considering that $[\mathbf{C}(\mathbf{u})]_{ii}$ has a (1, 1)-th 674 zero element, i.e., $[C_{11}(\Phi \bar{\mathbf{u}})]_{ii} = 0$, and that if $k \neq l$ then $i \notin \mathcal{V}_l$ and thus $\varphi_i^l = \mathbf{0}$, it follows 675 that for some index $i \in \mathcal{V}_k$,

$$\varphi_i^{k+} [\mathbf{C}(\Phi \bar{\mathbf{u}})]_{ii} \varphi_i^l = \varphi_i^{k+} [\mathbf{C}(\Phi \bar{\mathbf{u}})]_{ii} \varphi_i^k = \frac{|E_i|}{|\Omega_k|} [C_{11}(\Phi \bar{\mathbf{u}})]_{ii} = 0 \quad (61)$$

676 The matrix $[\Phi^+ \mathbf{C}(\Phi \bar{\mathbf{u}}) \Phi]_{kl} = 0$ for all $k, l = 1, 2, \dots, N$, and thus,

$$\bar{\mathbf{C}}(\bar{\mathbf{u}}) = \Phi^+ \mathbf{C}(\Phi \bar{\mathbf{u}}) \Phi = \mathbf{0} \quad (62)$$

677 as indicated by the LCM in eq. (11).

678 **A.2.2 Magnitude Analysis for Residual Dynamics**

679 Next, the magnitude of the residual dynamics $\mathbf{r}^{(2)}(\mathbf{u}, t)$ is analyzed to pinpoint the missing
680 physics in the LCM. By definition,

$$\mathbf{r}^{(2)}(\mathbf{u}, t) = \dot{\bar{\mathbf{u}}} - \mathbf{r}^{(1)}(\bar{\mathbf{u}}, t) \quad (63a)$$

$$= \Phi^+ \mathbf{r}(\mathbf{u}, t) - \mathbf{r}^{(1)}(\mathbf{u}, t) \quad (63b)$$

$$= \underbrace{\Phi^+ \mathbf{A}^{-1} \mathbf{B} \mathbf{u} - \bar{\mathbf{A}}(\mathbf{w})^{-1} \bar{\mathbf{B}}(\mathbf{w}) \bar{\mathbf{u}}}_{\#1} + \underbrace{\Phi^+ \mathbf{A}^{-1} \mathbf{C}(\mathbf{u}) \mathbf{u} - \bar{\mathbf{A}}(\mathbf{w})^{-1} \bar{\mathbf{C}}(\bar{\mathbf{u}}) \bar{\mathbf{u}}}_{\#2} \quad (63c)$$

$$+ \underbrace{\Phi^+ \mathbf{A}^{-1} \mathbf{f}(t) - \bar{\mathbf{A}}(\mathbf{w})^{-1} \bar{\mathbf{f}}(t)}_{\#3}$$

681 The magnitude analysis for terms $\#1$ and $\#3$ can be found in Ref. [18]. The analysis for
682 term $\#2$ is presented next. Let $\mathbf{D}(\bar{\mathbf{u}}) = \mathbf{A}^{-1} \mathbf{P} \mathbf{C}(\Phi \bar{\mathbf{u}})$ so that,

$$\Phi^+ \mathbf{A}^{-1} \mathbf{C}(\mathbf{u}) \mathbf{u} - \bar{\mathbf{A}}(\mathbf{w})^{-1} \bar{\mathbf{C}}(\bar{\mathbf{u}}) \bar{\mathbf{u}} \quad (64a)$$

$$= \Phi^+ \mathbf{A}^{-1} \mathbf{C}(\mathbf{u}) \mathbf{u} - \Phi^+ \mathbf{A}^{-1} \mathbf{P} \mathbf{C}(\Phi \bar{\mathbf{u}}) \Phi \Phi^+ \mathbf{u} \quad (64b)$$

$$= \Phi^+ \mathbf{A}^{-1} \mathbf{C}(\mathbf{u}) \mathbf{u} - \Phi^+ \mathbf{D}(\bar{\mathbf{u}}) \Phi \Phi^+ \mathbf{u} \quad (64c)$$

$$(64d)$$

683 where $\mathbf{P} = \Phi \Phi^+$. Thus,

$$\|\Phi^+ \mathbf{A}^{-1} \mathbf{C}(\mathbf{u}) \mathbf{u} - \bar{\mathbf{A}}(\mathbf{w})^{-1} \bar{\mathbf{C}}(\bar{\mathbf{u}}) \bar{\mathbf{u}}\| \quad (65a)$$

$$\leq \|\Phi^+ \mathbf{A}^{-1} \mathbf{C}(\mathbf{u}) \mathbf{u} - \Phi^+ \mathbf{D}(\bar{\mathbf{u}}) \mathbf{u}\| + \|\Phi^+ \mathbf{D}(\bar{\mathbf{u}}) \mathbf{u} - \Phi^+ \mathbf{D}(\bar{\mathbf{u}}) \Phi \Phi^+ \mathbf{u}\| \quad (65b)$$

$$\leq \|\Phi^+\| \underbrace{\|\mathbf{A}^{-1} \mathbf{C}(\mathbf{u}) \mathbf{u} - \mathbf{D}(\bar{\mathbf{u}}) \mathbf{u}\|}_{\#1} + \|\Phi^+ \mathbf{D}(\bar{\mathbf{u}})\| \underbrace{\|\mathbf{u} - \Phi \Phi^+ \mathbf{u}\|}_{\#2} \quad (65c)$$

684 where term $\#2$ is due to the approximation of non-uniform temperature as constants, and
685 term $\#1$ is the error in the advection dynamics due to coarse-graining.

686 **A.3 Lumped Capacitance Model**

687 The following assumptions are employed: (1) the temperature in component (i) is described
688 by a scalar time-varying average temperature $\bar{u}^{(i)}$, (2) between neighboring components (i)
689 and (j) the heat flux is approximated as,

$$q_{ij} = \frac{\bar{u}^{(j)} - \bar{u}^{(i)}}{R_{ij}} \quad (66)$$

690 where R_{ij} is the thermal resistance. Empirically, for a component of isotropic heat conduc-
691 tivity k , length ℓ , and cross-section area A , the thermal resistance is $R = \ell/kA$. Between
692 components i and j , define $R_{ij} = R_i + R_j$. In addition, the heat flux due to Dirichlet
693 boundary condition is computed as $q_{iT} = (T_b - \bar{u}^{(i)})/R_i$.

694 At component i , the dynamics of LCM are given by,

$$\int_{E_i} \rho c_p \dot{\bar{u}}^{(i)} dE_i = \left(\sum_{j \in \mathcal{N}_i} \int_{e_{ij}} \frac{\bar{u}^{(j)} - \bar{u}^{(i)}}{R_{ij}} de_{ij} \right) + \int_{e_{iq}} q_b de_{iq} + \int_{e_{iT}} \frac{T_b - \bar{u}^{(i)}}{R_i} de_{iT} \quad (67a)$$

$$\bar{A}^{(i)} \dot{\bar{u}}^{(i)} = \left(\sum_{j \in \mathcal{N}_i} \frac{|e_{ij}|}{R_{ij}} (\bar{u}^{(j)} - \bar{u}^{(i)}) \right) + |e_{iq}| \bar{q}^{(i)} + \frac{|e_{iT}|}{R_i} (\bar{T}^{(i)} - \bar{u}^{(i)}) \quad (67b)$$

$$= \sum_{j \in \mathcal{N}_i} \left(-\frac{|e_{ij}|}{R_{ij}} \bar{u}^{(i)} + \frac{|e_{ij}|}{R_{ij}} \bar{u}^{(j)} \right) + \left(-\frac{|e_{iT}|}{R_i} \bar{u}^{(i)} \right) + \left(|e_{iq}| \bar{q}^{(i)} + \frac{|e_{iT}|}{R_i} \bar{T}^{(i)} \right) \quad (67c)$$

$$= \sum_{j \in \mathcal{N}_i \cup \{T_b\}} \left(\bar{B}_{ij}^{(i)} \bar{u}^{(i)} + \bar{B}_{ij}^{(j)} \bar{u}^{(j)} \right) + \bar{f}^{(i)} \quad (67d)$$

695 where in eq. (67b) $|e|$ denotes the length ($d = 2$) or area ($d = 3$) of a component boundary
696 e . The $\bar{A}^{(i)}$, $\bar{B}_{ij}^{(i)}$, and $\bar{B}_{ij}^{(j)}$ quantities are provided in eq. (14).

697 The lumped-mass representation for the four-component TPS is shown in Fig. ???. Let
698 v_i represent the area of the i -th element, $\overline{\rho c_p}_i$, the heat capacity evaluated using the average
699 temperature $\bar{u}^{(i)}$, and $1/R_{ij} = 1/R_i(\bar{u}^{(i)}) + 1/R_j(\bar{u}^{(j)})$ the equivalent thermal resistance
700 between elements i and j . Leveraging the formulas from eqs. (13) and (14), the LCM
701 matrices are given by,

$$\bar{\mathbf{A}} = \begin{bmatrix} \overline{\rho c_p}_1 v_1 & 0 & 0 & 0 \\ 0 & \overline{\rho c_p}_2 v_2 & 0 & 0 \\ 0 & 0 & \overline{\rho c_p}_3 v_3 & 0 \\ 0 & 0 & 0 & \overline{\rho c_p}_4 v_4 \end{bmatrix}, \quad (68a)$$

$$\bar{\mathbf{B}} = \begin{bmatrix} \frac{1}{R_{12}} + \frac{1}{R_{14}} & -\frac{1}{R_{12}} & 0 & -\frac{1}{R_{14}} \\ -\frac{1}{R_{12}} & \frac{1}{R_{12}} + \frac{1}{R_{24}} + \frac{1}{R_{23}} & -\frac{1}{R_{23}} & -\frac{1}{R_{24}} \\ 0 & -\frac{1}{R_{32}} & \frac{1}{R_{32}} + \frac{1}{R_{34}} & -\frac{1}{R_{34}} \\ -\frac{1}{R_{14}} & -\frac{1}{R_{24}} & -\frac{1}{R_{34}} & \frac{1}{R_{14}} + \frac{1}{R_{24}} + \frac{1}{R_{34}} \end{bmatrix}, \quad \bar{\mathbf{f}} = \begin{bmatrix} \bar{q}^{(1)} \\ \bar{q}^{(2)} \\ \bar{q}^{(3)} \\ 0 \end{bmatrix} \quad (68b)$$

702 References

- 703 [1] Adam J. Amar, A. Brandon Oliver, Benjamin S. Kirk, Giovanni Salazar, and Justin
704 Drob. Overview of the charring ablator response (char) code. In AIAA, editor, *AIAA
705 Aviation Forum*, 2016.
- 706 [2] Guy L. Bergel, Frank B. Beckwith, Gabel J. de Frias, Kevin M. Manktelow, Mark T.
707 Merewether, Scott T. Miller, Krishen J. Parmar, Timothy S. Shelton, Jesse T. Thomas,
708 Jeremy T. Trageser, Benjamin T. Treweek, Michael V. Veilleux, and Ellen B. Wagman.
709 *Sierra/SolidMechanics 5.6 User's Manual*, 2022.
- 710 [3] Ricky T. Q. Chen, Yulia Rubanova, Jesse Bettencourt, and David Duvenaud. Neural
711 ordinary differential equations, 2019.

- [4] Jonathan Clausen, Victor Brunini, Lincoln Collins, Robert C Knaus, Alec Kucala, Stephen Lin, Daniel Robert Moser, Malachi Phillips, Thomas Michael Ransegrenola, Samuel Ramirez Subia, et al. Sierra multimechanics module: Aria verification manual-version 5.22. Technical report, Sandia National Lab.(SNL-NM), Albuquerque, NM (United States), 2024.
- [5] Gary Cohen and Sebastien Pernet. *Finite Element and Discontinuous Galerkin Methods for Transient Wave Equations*. Springer Dordrecht, Le Chesnay and Toulouse France, 2018.
- [6] Jianhao Fang, Weifei Hu, Zhenyu Liu, Yuhao Zhou, Chao Wei, and Jianrong Tan. A reduced order finite element-informed surrogate model for approximating global high-fidelity simulations. *Structural and Multidisciplinary Optimization*, 67(12), 2024.
- [7] Matthew Gasch, Keith Peterson, Mairead Stackpoole, Ethiraj Venkatapathy, Gregory Gonzales, and Kyle Hendrickson. Development of advanced ablative carbon phenolic tps for future nasa missions and commercial space. In *38th Annual Small Satellite Conference*, Logan, Utah, May 2024.
- [8] Micah A. Howard and Ben F. Blackwell. A multi-dimensional finite element based solver for decomposing and non-decomposing thermal protection systems. In AIAA, editor, *AIAA Aviation Forum*, 2015.
- [9] Frank P. Incropera, David P. DeWitt, Theodore L. Bergman, and Adrienne S. Lavine. *Fundamentals of Heat and Mass Transfer*. Wiley, Hoboken, NJ, 7th edition, 2011.
- [10] R. J. Klock and Carlos Cesnik. Nonlinear thermal reduced-order modeling for hypersonic vehicles. *AIAA Journal*, 55(7), 2017.
- [11] Arun Govind Neelan. Linear and non-linear reduced order model of scramjet. In *Advances in Multidisciplinary Design, Analysis and Optimization*, pages 111–118, Singapore, 2025.
- [12] Alberto Padovan, Blaine Vollmer, Francesco Panerai, Marco Panesi, Kelly A. Stephani, and Daniel J. Bodony. An extended bformulation for ablating-surface boundary conditions. *International Journal of Heat and Mass Transfer*, 218:124770, 2024.
- [13] Eric Parish and Karthik Duraisamy. Non-markovian closure models for large eddy simulations using the mori-zwanzig formalism. *Phys. Rev. Fluids*, 2:014604, Jan 2017.
- [14] Eric Parish and Karthik Duraisamy. A unified framework for multiscale modeling using the mori-zwanzig formalism and the variational multiscale method. *ArXiv*, 12 2017.
- [15] Eric Parish and Karthik Duraisamy. *Coarse-Graining Turbulence Using the Mori-Zwanzig Formalism*. Cambridge University Press, Cambridge, 2025.
- [16] Carl Edward Rasmussen and Christopher K. I. Williams. *Gaussian Processes for Machine Learning*. The MIT Press, 2006.

- 748 [17] Adam Thelen, Xiaoge Zhang, Olga Fink, Yan Lu, Sayan Ghosh, Byeng D. Youn,
749 Michael D. Todd, Sankaran Mahadean, Chao Hu, and Zhen Hu. A comprehensive
750 review of digital twin – part 1: modeling and twinning enabling technologies. *Structural*
751 and *Multidisciplinary Optimization*, 65(12), 2022.
- 752 [18] Carlos A. Vargas Venegas, Daning Huang, Patrick Blonigan, and John Tencer. Physics-
753 infused reduced-order modeling for analysis of multi-layered hypersonic thermal protec-
754 tion systems, 2025.
- 755 [19] Yongyong Xian, Baisong Pan, and Luping Luo. A new model updating strategy with
756 physics-based and data-driven models. *Structural and Multidisciplinary Optimization*,
757 64(1), 2021.
- 758 [20] Yin Yu, John Harlim, Daning Huang, and Yan Li. Learning coarse-grained dynamics
759 on graph. *arXiv preprint arXiv:2405.09324*, 2024.